# Direct Test of Supercooled Liquid Scaling Relations

T. Hecksher,[1, a)] D. H. Torchinsky,[2, a)] C. Klieber,[3, a)] J. A. Johnson,[3, a)] J. C. Dyre,[4] and Keith A. Nelson[3]
[1)] *Glass and Time, IMFUFA, Dept. of Science and Environment, Roskilde University, DK-4000 Roskilde, Denmark*
[2)] *Department of Physics, MIT, Cambridge, MA 02139, USA*
[3)] *Department of Chemistry, MIT, Cambridge, MA 02139, USA*
[4)] *DNRF Centre Glass and Time, IMFUFA, Dept. of Sciences, Roskilde University, DK-4000 Roskilde, Denmark*

Diverse material classes exhibit practically identical behavior when made viscous upon cooling toward the glass transition, suggesting a common theoretical basis. The first-principles scaling laws that have been proposed to describe the evolution with temperature have yet to be appropriately tested due to the extraordinary range of time scales involved. We used seven different measurement methods to determine the structural relaxation kinetics of a prototype molecular glass former over a temporal range of 13 decades and over a temperature range spanning liquid to glassy states. For the material studied, our results comprise a comprehensive validation of the two scaling relations that are central to the fundamental question of whether supercooled liquid dynamics can be described universally. The ultrabroadband mechanical measurements demonstrated have fundamental and practical applications in polymer science, geophysics, multifunctional materials, and other areas.

arXiv:1701.01310v1 [cond-mat.soft] 5 Jan 2017

The extraordinary slowing down of viscous liquid dynamics upon cooling toward the glassy state plays a key role in myriad contexts including polymer processing, survival of living organisms in extreme cold, amorphous metal synthesis, and many others. Glass-forming liquids display a wide array of common features, despite quite different chemistry ranging from high-temperature covalently bonded glass formers to van der Waals liquids that typically form glasses below room temperature[1–6].

Viscoelastic relaxation behavior derives from two distinct and sequential processes common to all glass forming liquids. The primary or "alpha" structural relaxation dynamics, which dictate the time scales for molecular diffusion and flow, are non-exponential in time, typically extend over several decades of time scales at a single temperature, and shift dramatically from picoseconds at high temperatures and low viscosities to many seconds as the sample is cooled and the glassy state is approached. This behavior gives rise to broad loss peaks in elastic compliance spectra, covering an extended frequency range at any temperature and shifting from gigahertz to millihertz frequencies as the temperature is lowered (see Fig. 1). In addition to the temperature-dependent alpha relaxation dynamics for reorganization of intermolecular geometries, fast local rearrangements of molecules within existing "cage" geometries, the so-called "beta" relaxation processes, result in a higher-frequency feature in the loss spectrum. This is the simplest scenario, which appears to obtain when structural relaxation is slowed down through obstruction among neighboring molecules but not through extensive networks as in hydrogen-bonded liquids or entanglements as in polymers. In those more complicated cases, additional processes between these two can be observed[7,8]. For the present study, we chose a van der Waals molecular liquid in order to examine the universal alpha and beta relaxation processes without complications from additional dynamics.

A variety of empirical models[9–14], as well as the first-principles mode-coupling theory (MCT)[15,16], have been developed in an effort to rationalize the universal features of supercooled liquid dynamics. In its idealized form, MCT predicts for the local density dynamics a critical temperature $T_c$ at which there is a transition from ergodic behavior above $T_c$ to nonergodic behavior below, corresponding to arrest into a metastable glassy state. The theory predicts a scaling law referred to as "time temperature superposition" (TTS). TTS implies that the alpha relaxation spectrum retains the same width and shape as the temperature is changed, even as the frequency range varies widely. A wide range of practices in polymer processing, rheology, aging, and other areas are based on TTS[17–21], but it has never been tested directly for mechanical properties across most of the time scales spanned. TTS is consistent with earlier heuristic descriptions of supercooled liquids extending from high temperature all the way to the glass transition temperature. Mode-coupling theory also predicts distinct power-law scaling of alpha and beta relaxation processes at temperatures above $T_c$, with the dynamic exponents connected through arithmetic relations reminiscent of those associated with other critical phenomena. Thus, the seemingly disparate relaxation processes, separated by decades, are predicted to be intimately related.

The density dynamics of supercooled liquids could be characterized through measurement of the temperature-dependent elastic compliance spectrum, but due to various experimental challenges this has never been done over anywhere near the full frequency range of interest in a single material. Ultra-broadband dielectric measurements[22] and depolarized light scattering spectra[23] clearly show the alpha and beta relaxation features, but these techniques measure the dynamics of molecular dipoles or po-

[a)] These authors contributed equally.

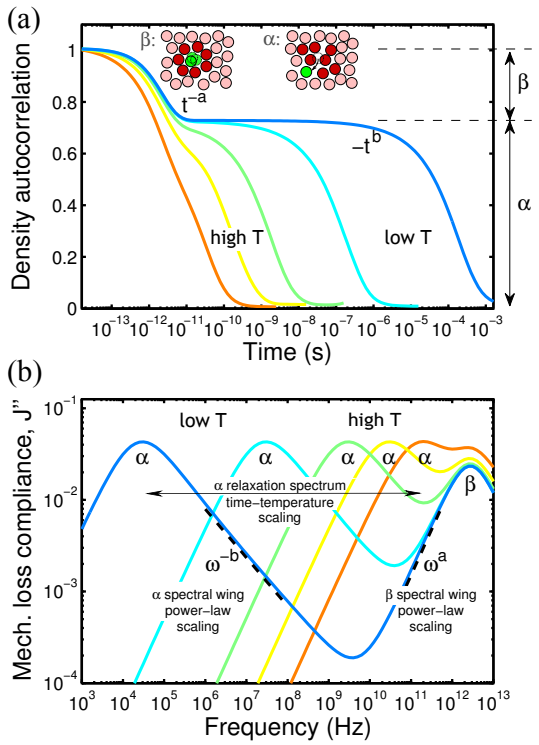


FIG. 1. Schematic depictions of primary (alpha) and fast (beta) relaxation processes in glass-forming liquids. Alpha and beta relaxation dynamics in (a) the time domain (density-density correlation function) and (b) the frequency domain (elastic compliance loss spectrum) at temperatures above the critical temperature $T_c$ predicted by mode-coupling theory (MCT). Time-temperature superposition is illustrated as the alpha relaxation spectral shape and width remain constant while the frequency range shifts by many decades as the temperature is varied. Dynamic critical exponents $a$ and $b$ describe the asymptotic power-law scaling of the relaxation kinetics predicted by MCT. At temperatures near $T_c$ there is a clear separation between alpha and beta relaxation time scales, with beta power-law relaxation of the density toward a time-independent "plateau" value followed eventually by alpha power-law relaxation kinetics. In the frequency domain, the relaxation spectral wings show corresponding power-law frequency dependences around a minimum in the compliance loss spectrum. The drawings in (a) show a schematic representation of the beta relaxation among multiple potential energy minima (the different locations sampled by the central molecule colored green) within pre-existing intermolecular geometries or "cages" (formed by the red-colored molecules) and alpha relaxation involving larger-scale rearrangement of the intermolecular geometries to permit molecular diffusion and flow.

larizabilities whose coupling to density is complicated and potentially temperature dependent. The key features of supercooled liquid structural relaxation dynamics that might reveal universal behavior at least within some classes of glass-forming materials (e.g., organic van der Waals liquids) have been tested through light scattering and neutron scattering spectra (see, e.g.,[24–28]), but not through direct measurement of density dynamics over a sufficient frequency range.

## I. EXPERIMENTS AND RESULTS

We used seven complementary methods, based on six experimental setups, to compile ultrabroadband longitudinal compliance spectra for the glass-forming liquid tetramethyl tetraphenyl trisiloxane (sold commercially as DC704). Four of the methods were photoacoustic techniques[29–33] through which acoustic waves in the frequency range 1 MHz–100 GHz were generated and detected optically. The corresponding acoustic wavelength range was $\sim$ 20 nm–2 mm. Longer acoustic wavelengths are comparable to sample sizes, so for lower frequencies in the range $\sim$ 1 mHz–100 kHz, dynamical mechanical analysis methods involving piezo-ceramics that shear or compress the entire sample[34–36] were used. The measurements spanned more than 13 orders of magnitude in frequency with less than three decades of gaps, yielding structural relaxation dynamics in the temperature range 200–320 K. Our earlier measurements in the low and high-frequency ranges[34,37] lacked sufficient frequency coverage for comprehensive testing of the scaling predictions, but the gap was bridged by the newly developed Nanosecond Acoustic Interferometry (NAI) method. The experimental methods and data analysis through which we determined the compliance spectra and the elastic modulus (the inverse of the compliance) are described in the online Supporting Information[33].

Figures 2(a) and 2(b) present the complex longitudinal modulus and compliance spectra of DC704 in the frequency range of approximately $10^{-3}$-$10^{11}$ Hz. The imaginary parts of the spectra have gaps in the ranges of approximately $10^{4}$-$10^{6}$ Hz and 1-10 GHz. In order to facilitate visualization of the temperature-dependent trends, the modulus and compliance spectra show only a subset of the data collected.

The primary temperature dependence, observed clearly in both real and imaginary components of the modulus spectra, is the movement of the alpha relaxation peak across about nine decades to lower frequencies as the temperature is reduced toward the glass transition temperature $T_g \approx 210$ K. At any given frequency $\omega_0$, the real part of the modulus $M(\omega_0, T)$ increases as the sample is cooled, reflecting the stiffening of the liquid as it approaches the glassy state. At any given temperature $T_0$, $M(\omega, T_0)$ plateaus at frequencies above those of the alpha relaxation spectrum, since at such high frequencies the liquid cannot undergo structural relaxation during the acoustic oscillation period, resulting in a solid-like response.

The compliance spectra show analogous behavior upon cooling: movement of the alpha relaxation spectrum across many decades and a decrease in the real part at low temperatures and high frequencies. The beta relax-

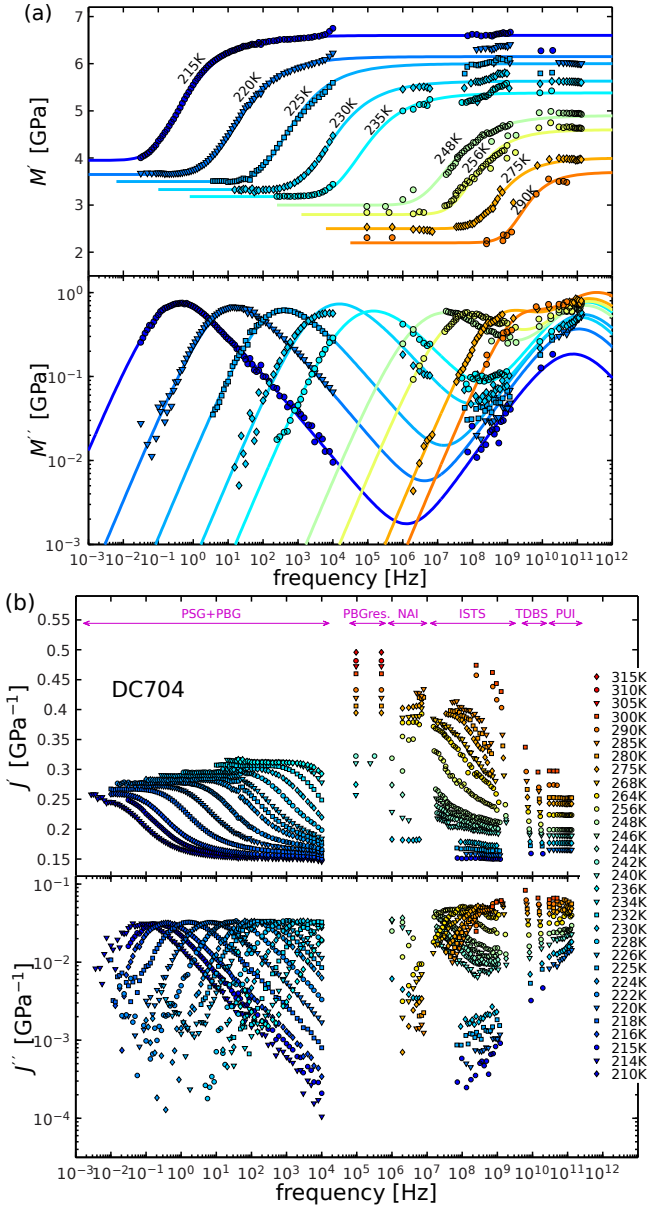


FIG. 2. (a) Longitudinal modulus spectra of DC704. Solid lines are guides to the eye. (b) Elastic compliance spectra of DC704. The techniques used in the different frequency ranges are indicated.

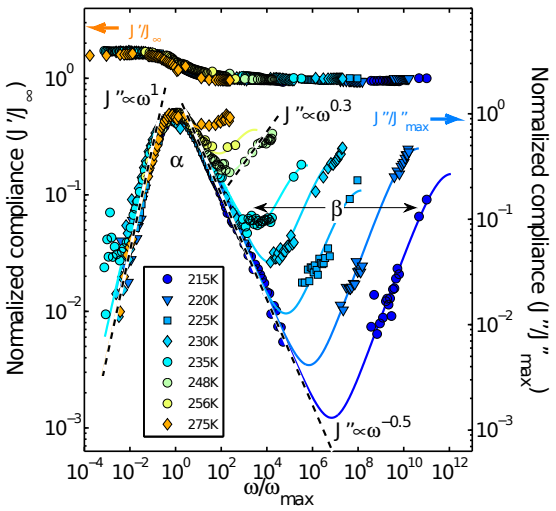


FIG. 3. Master plot of the compliance demonstrating time-temperature superposition. The individual traces are scaled and shifted according to the fit values. The low-frequency side of the imaginary part follows a linear power-law, $J'' \propto \omega^1$ (dashed line), corresponding to exponential long-time kinetics. The full curves give analytic model fits based on an alpha relaxation spectrum that follows an $\omega^{-0.5}$ high-frequency decay. The $\omega^{0.3}$ power-law also shown here corresponds to the value found to fit the beta relaxation spectral wing near the minimum at 248 K. (See Eq. 2 and Fig. 5)

ation feature is observed most clearly in the imaginary parts of the modulus and compliance functions, which both rise at high frequencies.

## II. SCALING ANALYSIS

Time-temperature superposition states that for the alpha relaxation dynamics, the normalized density autocorrelation function can be written as $\Phi(t,T) = F(t/\tau_\alpha(T))$, i.e., a single temperature independent form $F(t/\tau_\alpha(T))$ describes the relaxation dynamics at all temperatures, with the temperature dependence contained only in the values of the characteristic relaxation time $\tau_\alpha(T)$. In that case the alpha relaxation spectrum $J''(\omega)$ displays analogous behavior. In order to test TTS, we normalized the imaginary compliance spectra by the peak heights and the real spectra by the high-frequency limiting value $J_\infty$, and shifted both by amounts that made the peak frequencies in $J''(\omega)$ coincide. The results are shown in Fig. 3. The alpha relaxation features superpose well across the entire temperature regime studied. The imaginary parts have the characteristic asymmetric shape found for most glass-forming materials: the low-frequency sides of the alpha relaxation spectra follow the Maxwell behavior, $J''(\omega) \propto \omega^1$, while the high-frequency sides follow a power-law $J''(\omega) \propto \omega^{-1/2}$. The shifting of the spectra to make the alpha peaks overlap separates the beta relaxation features (which all appear at the high-frequency range in Fig. 2) on the scaled frequency axis. The scaled plots highlight the increase in separation between alpha and beta relaxations upon cooling.

Figure 4(a) shows the values of the characteristic relaxation time $\tau_\alpha$ of the alpha process as a function of temperature determined from fits to the stretched exponential function $\exp(-(t/\tau_\alpha)^n)$ with a temperature-independent stretching exponent $n$ and strongly temperature dependent $\tau_\alpha$ values. The stretching exponent

was fixed at $n = 0.5$, which at high frequencies corresponds to an $\omega^{-1/2}$ decay of the imaginary part of the compliance[4,38,39]. The observed non-Arrhenius temperature dependence is typical of glass-forming liquids and is associated generally with a complex energy landscape rather than a single activation energy for all relaxation processes[2–6,40]. The relaxation time data were fit to the MCT power-law prediction[15]

$$\tau_\alpha = \tau_x \left[T_c/(T - T_c)\right]^\gamma \tag{1}$$

with $\tau_x$ and $\gamma$ as free parameters. This prediction is for temperatures above $T_c$ (taken as 240 K as described below), although as suggested heuristically we find that TTS applies also below 240 K. The full set of $\tau_\alpha(T)$ values was fitted to the commonly used empirical Vogel-Fulcher-Tammann (VFT) function[41,42] $\tau_\alpha(T) = \tau_0 \exp\left[DT_0/(T - T_0)\right]$.

The MCT interpolation formula[43]

$$J''(\omega) = \frac{J''_{min}}{a+b}\left[a\left(\frac{\omega}{\omega_{min}}\right)^{-b} + b\left(\frac{\omega}{\omega_{min}}\right)^{a}\right] \tag{2}$$

connects the two relaxation features around the minimum between. This expression was fitted to the measured spectra in the region around the minimum. The fitted values for $a$ and $b$ are shown in Fig. 4(b). The uncertainty of the fits increases dramatically as the temperature increases due to the merging of the two processes making a distinction of the separate processes difficult. The MCT predicts a relation between the two exponents according to which

$$\lambda_a = \frac{\Gamma(1-a)^2}{\Gamma(1-2a)} = \lambda_b = \frac{\Gamma(1+b)^2}{\Gamma(1+2b)} \tag{3}$$

where $\Gamma(z)$ is the gamma-function defined as $\Gamma(z) = \int_0^\infty x^{z-1}e^{-x}dx$. The relation is tested in Fig. 4(c), which shows that the data are consistent with this prediction at temperatures above 240 K, but clearly breaks down below. We take this to define the MCT critical temperature. The value of the alpha relaxation time at $T_c$, $\tau_\alpha(240\text{ K}) \approx 0.1$ $\mu$s, is typical for $T_c$, below which idealized MCT breaks down[16] due to the onset of thermally assisted hopping[44–46] through which alpha relaxation continues to occur.

Figure 4(d) compares the alpha relaxation critical exponent $\gamma$ determined in Fig. 4(a) based on $T_c = 240$ K to the MCT prediction that connects the power-law exponents to $\gamma$ through the relation[15]

$$\gamma = 1/(2a) + 1/(2b)\,. \tag{4}$$

The above analysis indicates that MCT is valid at temperatures above 240 K for the studied liquid. For the fits to be useful as a test of the MCT predictions, there must be sufficient separation between the alpha and beta relaxation spectra as $T \to T_c$ from above that the $a$ and $b$ exponents can be associated distinctly with the two features[26,47]. This was the case for our results below 248 K and thus MCT can be meaningfully tested in the temperature range 240–248 K.

Figure 5 shows the region around the minima between the alpha and beta features of the compliance loss spectra $J''(\omega)$ at temperatures 240 K and 248 K. As a final test Eq. (2) was compared to the data with fixed exponent values. Only the minimum frequency $\omega_{\min}$ and the minimum compliance loss $J''_{\min}$ positions of each curve were adjusted to fit the data. The exponent value $b = 0.50$ was determined from the high-frequency wing of the alpha relaxation spectra evident in the TTS plot (Fig. 3). From this the predicted value of the exponent $a$ could be calculated using Eq. (3). This yielded the value $a = 0.28$, which should describe the low-frequency wing of the beta relaxation spectra. The resulting prediction completely determines the shape of the curves which go through the data well within the experimental scatter.

## III. CONCLUSIONS

Our measurements provide the first ultra-broadband mechanical relaxation spectra of a glass-forming liquid reaching the high frequencies of the beta relaxation spectrum and extending to the low frequencies of the alpha relaxation spectrum even as $T_g$ is approached. The results give direct experimental support for time-temperature superposition of the alpha relaxation spectrum above and below the MCT critical temperature (240 K), the validity of which is often assumed in empirical studies of glass-forming liquids and in modeling used for practical applications. Our results also permitted calculation of the dynamic critical exponents of MCT above $T_c$, yielding results consistent with predictions that relate the alpha and beta relaxation dynamics. In continuing work, we are filling in the frequency gaps of just under three decades within the more than 13 decades that the present measurements cover. We are also extending the measurements to higher frequencies in order to improve the reliability of our tests. We also have measured shear relaxation dynamics across a wide frequency range[37], and filling in the frequency gaps for these measurements will permit comparison between longitudinal and shear dynamics that may show distinct temperature-dependent behavior[48].

DC704 is the first sample for which mechanical relaxation dynamics have been measured across the frequency range we have explored. Additional glass-forming liquids must be examined in order to assess the generality of TTS and other MCT predictions. Our results demonstrate that access is now available to the extraordinarily wide frequency range needed for such comprehensive tests of supercooled liquids and a wide range of partially disordered materials including relaxor ferroelectrics, block copolymers, and many others.

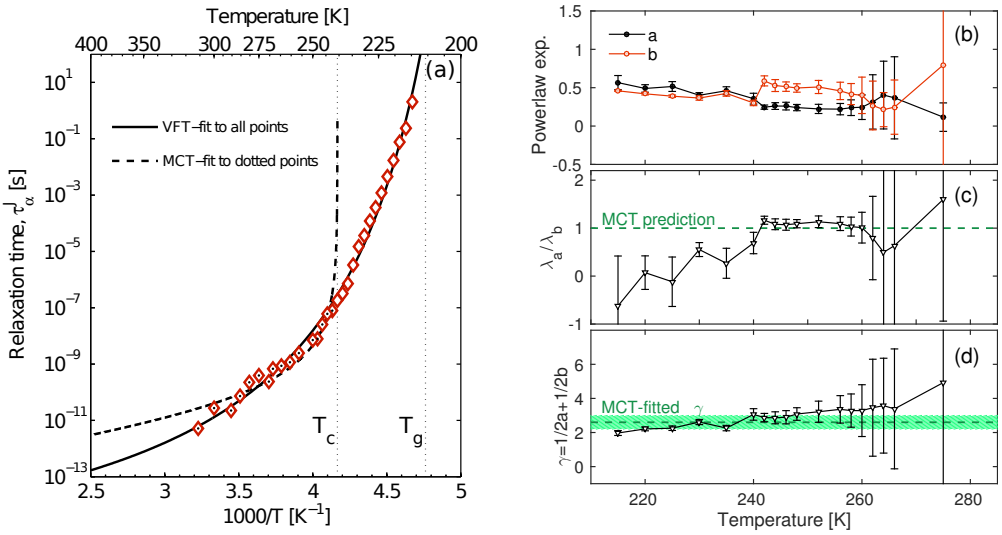


FIG. 4. (a) The characteristic alpha relaxation time plotted as a function of inverse temperature where the Arrhenius equation gives a straight line. The glass transition temperature is at $T_g \cong 210$ K. The VFT equation was fitted to all data points (full line) yielding $\log \tau_0 = -15.0 \pm 0.8$, $D = 6 \pm 1$ and $T_0 = 183 \pm 5$ K. The MCT critical temperature $T_c = 240$ K was identified from (b) as the temperature below which MCT predictions clearly break down; the MCT power-law fit to the high-temperature points ($T > T_c$) (marked by central black dots) yielded the following fit parameters: $\log(\tau_x/\mathrm{s}) = -12.0 \pm 0.5$, $\gamma = 2.7 \pm 0.4$. (b) Values of powerlaw exponents $a$ and $b$ over a wide temperature range, determined as fitting parameters to Eq. (3). (c) Test of the MCT prediction in Eq. (3) that $\lambda_a = \lambda_b$. The test is useful over the 240–248 K temperature range. (d) The calculated exponent $\gamma$ as a function of temperature. The green dotted line shows the value of obtained from fitting Eq. (1) to the relaxation times (in (d)) and the green area gives the estimated uncertainty on this value.

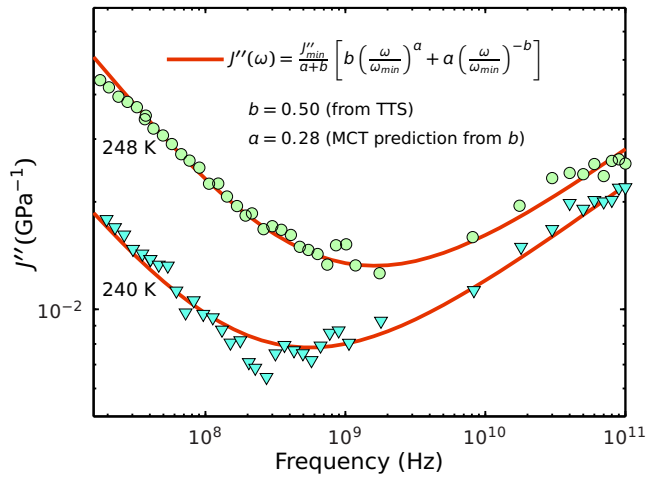


FIG. 5. Data around the minimum of the imaginary part of the compliance function fitted to the MCT power-law relation, Eq. 2, without adjustable shape parameters (critical exponents $a$ and $b$) at sample temperatures of 240 K and 248 K. The exponent $b = 0.50$ was determined from the low-temperature data using time-temperature superposition; Eq. 3 then yielded $a = 0.28$.

## IV. MATERIALS AND METHODS

### A. Overview

The seven different measurement methods and the frequency ranges that they cover are summarized in Fig. S1; detailed descriptions of the techniques and data collected from them are discussed in the Supporting Information[33]. The techniques include three low-frequency methods involving piezo-ceramics that shear or compress the entire sample quasi-statically[34–36,49] and four higher-frequency methods utilizing short laser pulses to excite and subsequently detect acoustic waves in an irradiated region[30–32,50–53].

The two lowest-frequency methods determine the complex frequency-dependent bulk modulus $K(\omega)$ and shear modulus $G(\omega)$ directly, where $\omega$ is the angular frequency. The longitudinal modulus is then given by $M(\omega) = M'(\omega) + iM''(\omega) = K(\omega) + (4/3)G(\omega)$. The four methods covering MHz-GHz frequencies determine acoustic parameters. The complex longitudinal modulus is given from the acoustic data as $M(\omega, T) = \rho(T)(c_L(\omega, T))^2$ where $\rho(T)$ is the temperature-dependent density and $c_L(\omega, T)$ the complex frequency-dependent longitudinal sound velocity.

In order to determine the modulus as a function of temperature from the sound velocity and damping rate, the thermal contraction of the sample must be accounted

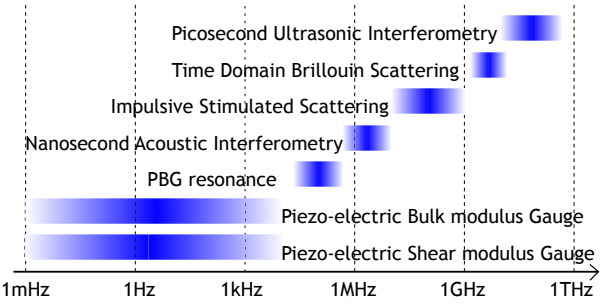


FIG. 6. Survey of mechanical spectroscopic techniques. At low frequencies (from mHz up to $\sim 10$ kHz) the piezo-electric Shear modulus Gauge (PSG) and the piezo-electric bulk modulus Gauge (PBG) were used to measure the shear and bulk moduli. Analysis of the overtones in the PBG provided access to some data points in the $100-500$ kHz region. In the low MHz range, nanosecond acoustic interferometry (NAI) was used to probe the frequency dependence of the longitudinal sound speed and attenuation rates directly. In the higher MHz range, impulsive stimulated scattering (ISS) was used to measure longitudinal sound velocities and damping at specified acoustic wavevectors. Finally, time-domain Brillouin light scattering (TDBS) and picosecond ultrasonic interferometry (PUI) were used to measure longitudinal acoustic speeds and attenuation in the MHz-GHz frequency ranges shown.

for. Using literature data of the thermal expansion coefficient $\alpha = 7.2\times10^{-4}[\mathrm{K}^{-1}]$[54,55] and assuming this quantity is temperature independent, the following expression for the temperature dependence of the density can be derived[37].

$$\begin{aligned}\rho(T) &= \frac{\rho(T_{ref})}{1+\alpha_p(T-T_{ref})} \\ &= \frac{1.07\ [\mathrm{kg/m^3}]}{1+7.2\times10^{-4}\ [\mathrm{K}^{-1}]\,(\mathrm{T}-298[\mathrm{K}])}\end{aligned} \tag{5}$$

Once the modulus is obtained, the complex longitudinal compliance is given by $J(\omega) = 1/M(\omega) = J'(\omega) - iJ''(\omega)$.

MCT relations are predictions for the mechanical susceptibility $\chi(\omega)$ to which $J(\omega)$ is proportional. Strictly speaking, $\chi(\omega)$ is related to the density autocorrelation function and therefore to the bulk compliance, not the longitudinal compliance. However, the difference between $K(\omega)$ and $M(\omega)$ (and thus also the bulk and longitudinal compliances) is negligible because the shear modulus is considerably smaller than the longitudinal modulus, and their frequency-dependent dynamics are very similar at both low[34,56,57] and high[48] frequencies.

### B. Sample Preparation

For the PSG, PBG, and ISS measurements, DC704 was obtained from Sigma Aldrich and used without purification. For the ISS measurements, the liquid was transferred into the cell through a 0.22 $\mu$m millipore filter into a fused quartz cuvette. During the ISS measurements, the sample was observed to become slightly opaque at the coldest temperatures. This is likely due to phase separation of dissolved impurities from the base liquid and disappeared when the liquid was reheated. The problem was overcome in subsequent experiments by mixing the sample with anhydrous $MgSO_4$, combined with heating under vacuum before filtration. This approach was adopted for the NAI, TDBS, and PUI techniques. Comparison of data both with and without treatment by the drying agent showed no difference in the acoustic parameters. The DC704 samples never crystallized during the course of our experiments.

The transducer techniques utilize home-built closed-cycle cryostats capable of keeping the temperature constant within a $\sim 5$ mK[58], while the NAI and ISS measurements were performed in a commercially available cold-finger cryostat. In these measurements, temperature sensing was provided by a factory calibrated platinum resistors immersed in the liquid a few millimeters away from the optical beams. The TDBS and PUI techniques were performed in a commercial sample-in-vapor cryostat and the temperature was monitored at a position a few millimeters away from the sample.

We did not carry out any calibration of temperatures between the cryostats of the different labs. However, the low-frequency part of the longitudinal spectrum was obtained as the sum of two individual measurements, which were carried out in the same experimental set-up (same cryostat, same electronics). We estimate that the uncertainty on the absolute temperature is less than the overall noise in the high-frequency methods.

## ACKNOWLEDGMENTS

The work at MIT was supported in part by National Science Foundation Grant No. CHE-1111557 and Department of Energy Grant No. DE-FG02-00ER15087. The work at Roskilde University was sponsored by the DNRF Grant no 61.

[1] Kauzmann, W. (1948) The nature of the glassy state and the behavior of liquids at low temperatures. *Chemical Review* **43**, 219–256.
[2] Angell, C. A. (1995) Formation of glasses from liquids and biopolymers. *Science* **267**, 1924–1935.
[3] Debenedetti, P. G. (1996) *Metastable liquids : concepts and principles.* (Princeton, N.J. : Princeton University Press).
[4] Dyre, J. C. (2006) Solidity of viscous liquids. IV. density fluctuations. *Phys. Rev. E* **74**, 021502.
[5] Roland, C. M. (2010) Relaxation phenomena in vitrifying polymers and molecular liquids. *Macromolecules* **43**, 7875–7890.
[6] Berthier, L & Biroli, G. (2011) Theoretical perspective on the glass transition and amorphous materials. *Rev. Mod. Phys.* **83**, 587.
[7] Johari, G. P & Goldstein, M. (1970) Viscous Liquids and the Glass Transition. II. Secondary Relaxations in Glasses of Rigid Molecules. *J. Chem. Phys.* **53**, 2372.
[8] Johari, G. P. (1982) Effect of annealing on the secondary relaxations in glasses. *J. Chem. Phys.* **77**, 4619–4626.
[9] Dyre, J. C. (2006) The glass transition and elastic models of glass-forming liquids. *Reviews of Modern Physics* **78**, 953–972.

[10]Gibbs, J. H & DiMarzio, E. A. (1958) Nature of the glass transition and the glassy state. *J. Chem. Phys.* **28**, 373–383.

[11]Cohen, M. H & Grest, G. S. (1979) Liquid-glass transition, a free volume approach. *Phys. Rev. B* **20**, 1077–1098.

[12]Kivelson, D, Kivelson, S. A, Zhao, X. L, Nussinov, Z, & Tarjus, G. (1995) A thermodynamic theory of supercooled liquids. *Physica A* **219**, 27–38.

[13]Jung, Y, Garrahan, J. P, & Chandler, D. (2005) Dynamical exchanges in facilitated models of supercooled liquids. *J. Chem. Phys.* **123**.

[14]Tripathy, M & Schweizer, K. S. (2009) The influence of shape on the glassy dynamics of hard nonspherical particle fluids. II. barriers, relaxation, fragility, kinetic vitrification, and universality. *J. Chem. Phys.* **130**, 244907.

[15]Götze, W & Sjögren, L. (1992) Relaxation processes in supercooled liquids. *Rep. Prog. Phys.* **55**, 241–376.

[16]Das, S. P. (2004) Mode-coupling theory and the glass transition in supercooled liquids. *Rev. Mod. Phys.* **76**, 785–851.

[17]Ferry, J. D. (1980) *Viscoelastic properties of polymers.* (John Wiley & Sons, Inc).

[18]Plazek, D. J. (1996) 1995 Bingham Medal Address: Oh, thermorheological simplicity, wherefore art thou? *Journal of Rheology* **40**, 987.

[19]Olsen, N. B, Christensen, T, & Dyre, J. C. (2001) Time-temperature superposition in viscous liquids. *Phys. Rev. Lett.* **86**, 1271–1274.

[20]Narayanaswamy, O. S. (1971) A model of structural relaxation in glass. *J. Am. Ceram. Soc.* **54**, 491–498.

[21]Moynihan, C. T, Easteal, A. J, DeBolt, M, & Tucker, J. (1976) Dependence of the fictive temperature of glass on cooling rate. *American Ceramic Society* **59**, 12–16.

[22]Lunkenheimer, P, Schneider, U, Brand, R, & Loidl, A. (2000) Glassy dynamics. *Contemp. Phys.* **41**, 15–36.

[23]Petzold, N & Rössler, E. A. (2010) Light scattering study on the glass former o-terphenyl. *J. Chem. Phys.* **133**, 124512.

[24]Li, G, Du, W. M, Sakai, A, & Cummins, H. Z. (1992) Light-scattering investigation of $\alpha$ and $\beta$ relaxation near the liquid-glass transition of the molecular glass salol. *Phys. Rev. A* **46**, 3343–3356.

[25]Li, G, Du, W. M, Chen, X. K, Cummins, H. Z, & Tao, N. J. (1992) Testing mode-coupling predictions for $\alpha$ and $\beta$ relaxation in $(Ca_{0.4}K_{0.6}(NO_3)_{1.4}$ near the liquid-glass transition by light scattering. *Phys. Rev. A* **45**, 3867–3879.

[26]Götze, W. (1999) Recent tests of the mode-coupling theory for glassy dynamics. *J. Phys.: Condens. Matter* **11**, A1.

[27]Wuttke, J, Hernandez, J, Li, G, Coddens, G, Cummins, H. Z, Fujiara, F, Petry, W, & Sillescu, H. (1994) Neutron and light-scattering study of supercooled glycerol. *Phys. Rev. Lett.* **72**, 3052–3055.

[28]Shen, G. Q, Toulouse, J, Beaufils, S, Bonello, B, Hwang, Y. H, Finkel, P, Hernandez, J, Bertault, M, Maglione, M, Ecolivet, C, & Cummins, H. Z. (2000) Experimental studies of the liquid-glass transition in trimethylheptane. *Phys. Rev. E* **62**, 783–792.

[29]Yan, Y.-X & Nelson, K. A. (1987) Impulsive stimulated light scattering. I. General theory. *J. Chem. Phys.* **87**, 6240–6256.

[30]Silence, S. M, Duggal, A. R, Dhar, L, & Nelson, K. A. (1992) Structural and orientational relaxation in supercooled liquid triphenylphosphite. *J. Chem. Phys.* **96**, 5448–5459.

[31]Thomsen, C, Grahn, H, Maris, H, & Tauc, J. (1986) Surface generation and detection of phonons by picosecond light pulses. *Phys. Rev. B* **34**, 4129–4138.

[32]Choi, J. D, Feurer, T, Yamaguchi, M, Paxton, B, & Nelson, K. A. (2005) Generation of ultrahigh-frequency tunable acoustic waves. *Appl. Phys. Lett.* **87**, 081907.

[33](year?) See online supplementary information.

[34]Hecksher, T, Olsen, N. B, Nelson, K. A, Dyre, J. C, & Christensen, T. (2013) Mechanical spectrum of viscous liquids. I. Low-frequency bulk and shear moduli of DC704 and 5-PPE measured by piezoceramic transducers. *J. Chem. Phys.* **138**, 12A543.

[35]Christensen, T & Olsen, N. B. (1994) Determination of the frequency-dependent bulk modulus of glycerol using a piezoelectric spherical shell. *Phys. Rev. B* **49**, 15396–15399.

[36]Christensen, T & Olsen, N. B. (1995) A rheometer for the measurement of high shear modulus covering more than seven decades of frequency below 50 khz. *Rev. Sci. Instrum.* **66**, 5019–5031.

[37]Klieber, C, Hecksher, T, Pezeril, T, Torchinsky, D. H, Dyre, J. C, & Nelson, K. A. (2013) Mechanical spectra of viscous liquids. II. Gigahertz-frequency longitudinal and shear acoustic dynamics in glycerol and dc704 studied by time-domain brillouin scattering. *J. Chem. Phys.* **138**, 12A544.

[38]Barlow, A. J, Erginsav, A, & Lamb, J. (1967). *Proc. R. Soc. London, Ser. A* **298**, 461.

[39]Nielsen, A. I, Jakobsen, B, Niss, K, Olsen, N. B, Richert, R, & Dyre, J. C. (2009) Prevalence of approximate $\sqrt{t}$ relaxation for the dielectric $\alpha$ process in visous organic liquids. *J. Chem. Phys.* **130**, 154508.

[40]Böhmer, R, Ngai, K. L, Angell, C. A, & Plazek, D. J. (1993) Nonexponential relaxation in strong and fragile glass-formers. *J. Chem. Phys.* **99**, 4201.

[41]Vogel, H. (1921) Das Temperaturabhängigkeitsgesetz der Viskosität von Flüssigkeiten. *Phys. Z.* **22**, 645–646.

[42]Tammann, G. (1925) Glasses as supercooled liquids. *J. Soc. Glass Technol.* **9**, 166–185.

[43]Cummins, H. Z, Du, W. M, Fuchs, M, Götze, W, A.Latz, Li, G, & Tao, N. J. (1993) Light scattering spectroscopy of the liquid-glass transition: comparison with idealized and extended mode coupling theory. *Physica A: Statistical Mechanics and its Applications* **201**, 207 – 222.

[44]Goldstein, M. (1969) Viscous liquids and the glass transition: A potential energy barrier picture. *J. Chem. Phys.* **51**, 3728–3739.

[45]Debenedetti, P. G & Stillinger, F. H. (2001) Supercooled liquids and the glass transition. *Nature* **410**, 259–267.

[46]Schroeder, T. B, Sastry, S, Dyre, J, & Glotzer, S. C. (2000) Crossover to potential energy landscape dominated dynamics in a model glass-forming liquid. *J. Chem. Phys.* **112**, 9834–9840.

[47]Cummins, H. (1999) The liquid-glass transition: a mode-coupling perspective. *J. Phys.: Condens. Matter* **11**, A95.

[48]Torchinsky, D. H, Johnson, J. A, & Nelson, K. A. (2012) $\alpha$-scale decoupling of the mechanical relaxation and diverging shear wave propagation length scale in triphenylphosphite. *J. Chem. Phys.* **136**, 174509.

[49]Hecksher, T. (2010) Ph.D. thesis (Roskilde University).

[50]Johnson, J. A. (2011) Ph.D. thesis (Massachusetts Institute of Technology).

[51]Yan, Y.-X & Nelson, K. A. (1987) Impulsive stimulated light scattering. II. Comparison to frequency-domain light-scattering spectroscopy. *J. Chem. Phys.* **87**, 6257–6266.

[52]Torchinsky, D. H. (2008) PhD thesis (Massachusetts Institute of Technology, Cambridge, MA).

[53]Klieber, C. (2010) Ph.D. thesis (Massachusetts Institute of Technology).

[54]Orcutt, R. H. (1973) Interlot density variation of a siloxane manometer fluid. *Journal of Vacuum Science Technology* **10**, 506–506.

[55]Poulter, K. F & Nash, P. J. (1979) Interferometric oil micromanometer. *Journal of Physics E-Scientific Instruments* **12**, 931–936.

[56]Christensen, T & Olsen, N. B. (1994) Quasistatic measurements of the frequency-dependent bulk and shear modulus of supercooled liquids. *J. Non-Cryst. Solids* **172-174**, 362–364.

[57]Gundermann, D, Niss, K, Christensen, T, Dyre, J. C, & Hecksher, T. (2014) The dynamic bulk modulus of three glass-forming liquids. *J. Chem. Phys.* **140**, 244508.

[58]Igarashi, B, Christensen, T, Larsen, E. H, Olsen, N. B, Pedersen, I. H, Rasmussen, T, & Dyre, J. C. (2008) A cryostat and temperature control system optimized for measuring relaxations of glass-forming liquids. *Rev. Sci. Instrum.* **79**, 045105.

# Supplementary Material: Direct Test of Supercooled Liquid Scaling Relations.

## I. EXPERIMENTAL METHODS

Overview over the seven different measurement methods and the frequency ranges that they cover are summarized in Fig. S1; detailed descriptions of the techniques and data collected from them are discussed in the subsequent sections below. The techniques include three low-frequency methods involving piezo-ceramics that shear or compress the entire sample quasi-statically[S1–S4] and four higher-frequency methods utilizing short laser pulses to excite and subsequently detect acoustic waves in an irradiated region[S5–S11].

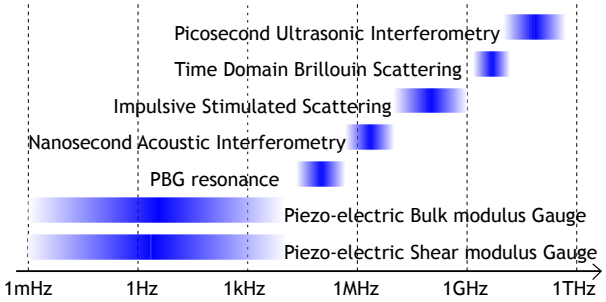


FIG. S1. Survey of mechanical spectroscopic techniques. At low frequencies (from mHz up to $\sim 10$ kHz) the piezo-electric Shear modulus Gauge (PSG) and the piezo-electric bulk modulus Gauge (PBG) were used to measure the shear and bulk moduli. Analysis of the overtones in the PBG provided access to some data points in the $100 - 500$ kHz region. In the low MHz range, nanosecond acoustic interferometry (NAI) was used to probe the frequency dependence of the longitudinal sound speed and attenuation rates directly. In the higher MHz range, impulsive stimulated scattering (ISS) was used to measure longitudinal sound velocities and damping at specified acoustic wavevectors. Finally, time-domain Brillouin light scattering (TDBS) and picosecond ultrasonic interferometry (PUI) were used to measure longitudinal acoustic speeds and attenuation in the MHz-GHz frequency ranges shown.

### A. Low-frequency methods

The low-frequency methods measure mechanical moduli directly. These techniques do not measure the longitudinal modulus, but the bulk and shear moduli. In the isotropic case (e.g., in a liquid) there are only two unique mechanical moduli, and the longitudinal modulus $M$ is given in terms of the bulk ($K$) and shear ($G$) moduli as: $M = K + 4/3G$.

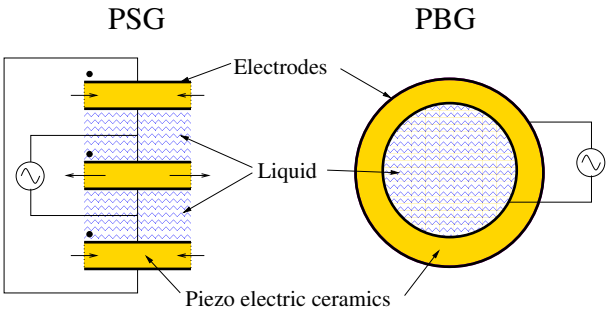


FIG. S2. Schematic drawing of the PSG and PBG. In the PSG three electrode-covered piezo-electric ceramic discs are mounted in a layer construction; the liquid is loaded into the gaps between the discs. In the PBG, a spherical shell of piezo-electric ceramic material is filled with the liquid via a hole drilled in the ceramics. A liquid reservoir (not shown here) is attached above the hole, allowing extra liquid to be drawn in as the temperature is lowered.

Both the piezo-electric shear modulus gauge (PSG) and the piezo-electric bulk modulus gauge (PBG) methods are based on the piezo-electric effect, i.e., the conversion of electrical to mechanical energy. These methods have been documented in detail by Christensen and Olsen in Refs. S3 and S2, respectively. In the following we briefly sketch the steps in modeling of the devices, which allow us to deduce a mechanical modulus from the electrical data.

### 1. Piezo-electric Shear Modulus Gauge

The PSG is constructed of three electrode-covered piezo-electric ceramic discs mounted in a layered construction, which prevents unwanted bending of the discs and further has the advantage that it can be mapped mathematically to a one-disc system involving a fixed wall[S3].

The liquid is loaded into the 0.5 mm gap between the discs (Fig. S2). Depending on the polarity of the discs as compared with the direction of an applied electric field, the discs expand or contract in the radial direction. Electrically, the middle disc is connected in parallel with the two outer discs in series as shown in Fig. S2. Here, the small dots indicate the polarity of the piezo-electric discs; thus when an electric field is applied, the middle disc moves in opposition to the two outer discs. With this construction the gap between the discs is field free, and the liquid is subjected to a purely mechanical perturbation.

The capacitance of each disc depends on its strain state, so if the liquid is partially clamping the disc (thus hindering its motion), the measured capacitance is lower than that of freely moving discs. By a precise measurement of the electrical capacitance of the PSG one can obtain the stiffness of the liquid in contact with the disc. In other words, knowing the exact relationship between the two, we can convert the electric impedance into the shear modulus.

The elasto-electric compliance matrix describes the connection between the components of the stress $\sigma_{ij}$ and strain $\epsilon_{ij}$ tensors and the electrical field of the piezo-electric material. The equations describing a axially polarized ceramic can be split into four independent parts, the relevant components of which can be reduced to the following

$$\begin{pmatrix} \sigma_{rr} \\ \sigma_{\phi\phi} \\ D_z \end{pmatrix} = \begin{pmatrix} c_{11} & c_{12} & -e_{13} \\ c_{12} & c_{11} & -e_{13} \\ e_{13} & e_{13} & \varepsilon_{33}^S \end{pmatrix} \begin{pmatrix} \epsilon_{rr} \\ \epsilon_{\phi\phi} \\ E_z \end{pmatrix} \tag{S1}$$

where $c_{11}$ and $c_{12}$ are elastic constants of the ceramic, $\epsilon_{33}^S$ is the dielectric constant, and $e_{13}$ is the coupling constant.

The measured capacitance $C_m$ of the disc can be found by integrating the charge density $D_z$ and dividing by the voltage

$$C_m = \frac{Q}{U} = \frac{\int_0^{r_0} 2\pi r D_z(r)\, dr}{\xi E_z}, \tag{S2}$$

where the charge density $D_z$ is given by Eq. (S1) and $\xi$ is the thickness of the disc. $D_z$ depends both on the strain state and the applied electrical field $E_z$. Evaluating this integral it is found that the capacitance is a function of the radial displacement at the edge of the disc $u_r(r_0)$

$$C_m = A u_r(r_0) + B \tag{S3}$$

where $A$ and $B$ are known constants. It remains to determine the displacement at the edge of the disc $u_r(r_0)$ as a function of rigidity of the liquid. The displacement $u_r$ is found by solving the radial equation of motion, which reduces to

$$c_{11}\left(r^2(u_r'') + u_r' - u_r\right) - \sigma_l \frac{r^2}{\xi} = -\omega^2 r^2 \rho u_r \tag{S4}$$

where the prime indicates the derivative with respect to $r$, $\xi$ is the thickness of the disc and $\sigma_l$ is the tangential stress that the liquid exerts on the disc. $\sigma_l$ is by definition proportional the shear modulus of the liquid $\sigma_l = G(\omega)u_r/d$, where $d$ is the thickness of the liquid layer (or equivalently the distance between the discs), which is the quantity relevant to determining the relaxation.

Figure S3 shows the measured capacitance of the empty (black trace) and liquid-filled (blue trace) PSG. At high temperatures there is no influence from the liquid at these frequencies and the two spectra are identical. The resonances in the spectrum are mechanical resonances of the discs. At lower temperatures, the shear modulus of the liquid increases and partially clamps the discs. This is observed as a drop in the capacitance below the first resonances. We will refer to the range of frequencies below the first resonance ($< 100$ kHz) of the system as the *quasi-static* region. The liquid also influences the positions of the overtones as compared with the spectrum of the empty device. In the quasi-static region, the shear modulus is found via the described inversion procedure. The inverted data, i.e., the inferred complex shear modulus, are shown in Fig. S4.

### 2. Piezo-electric Bulk Modulus Gauge

The PBG, which was also depicted in Fig. S2, consists of a spherical shell of a piezo-electric ceramic material polarized in the radial direction. The shell is covered by an electrode material both on the inside and the outside.

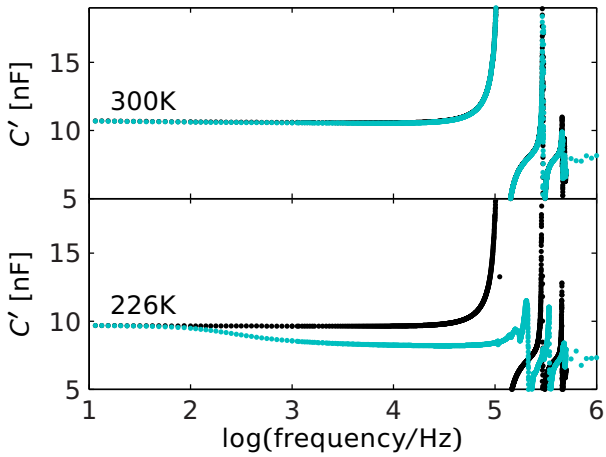


FIG. S3. Raw data of the empty (black) and liquid-filled (blue) PSG at two different temperatures. At 300 K the presence of the liquid does not affect the signal because the liquid is quite fluid. At 226 K the liquid partially clamps the discs, which is manifested as a drop in capacitance in the quasi-static region and a shift of the resonances in the high-frequency region.

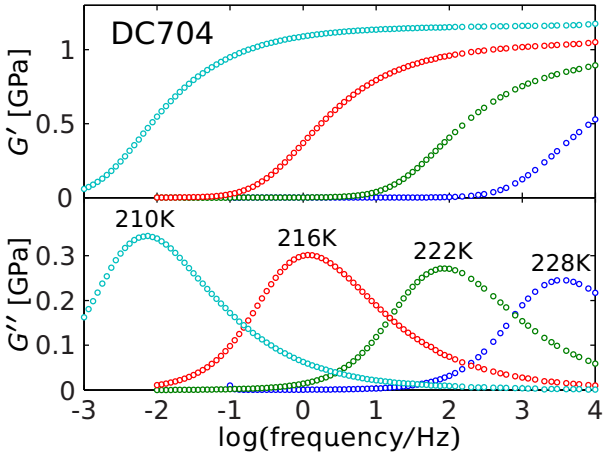


FIG. S4. Real and imaginary parts of the shear modulus of DC704 at four temperatures approaching $T_g$.

Applying an electric field to the capacitor, which these electrodes constitute, deforms the ceramic (expanding or contracting depending on the direction of the field) and effectively changes the inner volume of the sphere.

A liquid inside the shell will oppose this deformation and thus change the measured capacitance. The difference in capacitance between the empty, freely moving shell and the partially clamped shell can be related to the bulk modulus of the liquid. The deformation is radial. An analysis of forced vibrations in a visco-elastic sphere shows that in the low-frequency (quasi-static) region of the measurement this corresponds to an isotropic compression of the liquid, while at high frequencies it is a mixture of bulk and shear deformations.

In order to be able to fill the PBG with liquid, a hole is drilled in the shell. A tube is attached over the hole. Filling this tube, as well as the entire shell, allows the PBG to draw in extra liquid when the liquid in the shell contracts during cooling. Thus the liquid volume is constant throughout the duration of the measurement, i.e., at all temperatures.

The modeling of the PBG is somewhat simpler than that of the PSG since one can assume that the thickness of the ceramic is negligible in the direction of its motion. Thus we can express the model in terms of an electrical equivalent diagram, shown in Fig. S6, where the conversion from electrical to mechanical energy is modeled by a transducer $T_r$. On the electrical side of the diagram there is a capacitor $C_1$ which corresponds to the actual capacitor constituted by the two electrodes. On the mechanical side, the capacitor $C_2$ models the elastic properties of the ceramic, the inductor $L$ models the inertance, and the resistor $R$ models the friction. The "black box" $C_{\mathrm{liq}}$ is the liquid capacitance which is what we want to determine.

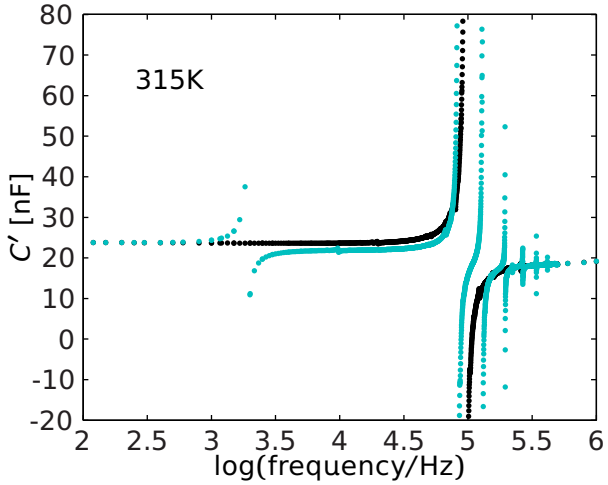


FIG. S5. Raw data of the empty (black) and the liquid-filled (blue) PBG. In the spectrum of the empty cell there is only one resonance (at $\sim$ 100 kHz). There are a number of extra features that all come from the liquid. At low frequencies the capacitance of the two is the same. Around 1 kHz there is a small resonance, which comes from the liquid flowing in and out of the shell via a tube. Above that resonance the shell is partially clamped and the measured capacitance is reduced compared to that of the empty PBG. At frequencies above the first big resonance, the extra resonances are all due to standing waves in the liquid.

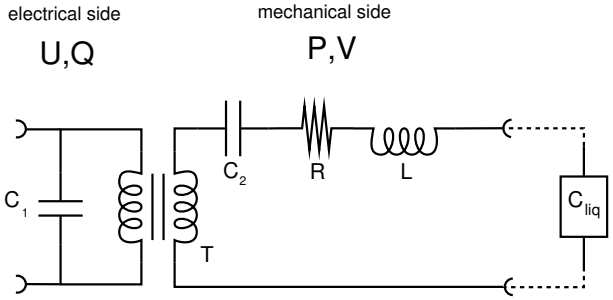


FIG. S6. Electrical equivalent model of the PBG. The transformer represents the conversion from electrical to mechanical energy in the piezo-electric ceramic. On the electric side of the network the capacitor is an actual capacitor that the electrodes constitute. On the mechanical side, an $LCR$ series models the inertial, elastic, and dissipative properties of the ceramic. When the PBG is empty the mechanical port is short circuited, allowing the shell to move freely. The liquid-filled PBG is modelled with an extra box $C_{\rm liq}$ in series.

The capacitance of the model depicted in Fig. S6 is given by

$$C_m(\omega) = C_1 + T_r^2 \frac{1}{\frac{1}{C_2} + i\omega R - \omega^2 L + \frac{1}{C_{\rm liq}}}. \tag{S5}$$

All the constants $C_1, C_2, L, R, T_r$ can be determined from a measurement of the empty PBG. A subsequent measurement of the liquid-filled PBG allows for the determination of the liquid's mechanical stiffness $S_{\rm liq} = 1/C_{\rm liq}$ by isolating that term.

Next, we wish to express the stiffness in terms of the elastic moduli. The mechanical stiffness is $S_{liq} = \delta p/\delta V \approx -\sigma_{rr}(r_0)/4\pi r_0^2 u_r$. Solving the equation of motion for forced vibrations in a visco-elastic sphere one finds the displacement field $u_r$, which leads to the following expression for the stiffness of the liquid[S2]

$$S_{\rm liq} = \frac{1}{V}\left[K - M\left(1 + \frac{1}{3}\frac{x^2 \sin x}{x\cos x - \sin x}\right)\right]. \tag{S6}$$

Here $V$ is the volume of the sphere, $K$ and $M$ are the (adiabatic) bulk and longitudinal moduli, and $x = \sqrt{\rho/M} r_0 \omega$. We have $S_{\rm liq} \to K/V$ as $\omega \to 0$, i.e., in the quasistatic region we are measuring the bulk modulus. The inverted complex bulk modulus data for DC704 are shown in Fig. S7.

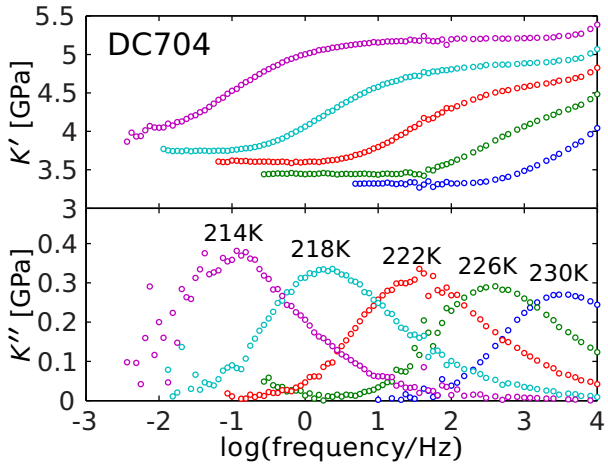


FIG. S7. Real and imaginary parts of the bulk modulus of DC704 for selected temperatures close to $T_g$.

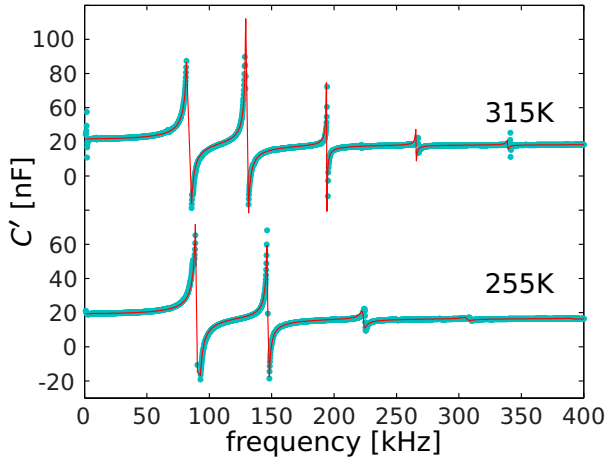


FIG. S8. Real part of capacitance in the resonance region of the PBG measurement. Data are blue dots and dashed lines are fits of a Eq. (S6) in combination with the model in Eq. (S5).

At high frequencies we can fit Eq. (S6) in conjunction with Eq. (S5) to the resonances, at least at high temperatures where we can assume $K = K(\omega \to 0) = M(\omega \to 0)$ and the viscosity to be frequency-independent. Fits to data in the resonance region are shown in Fig. S8.

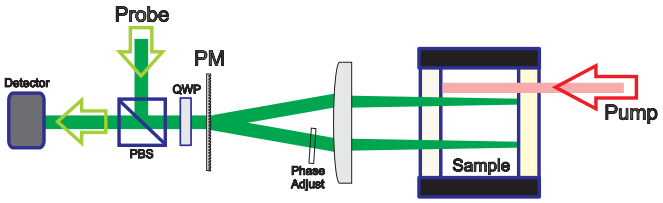


FIG. S9. Nanosecond acoustic interferometry setup. A pump pulse is absorbed weakly in the sample, and sudden heating and thermal expansion generate a cylindrical acoustic wave radiating outwards from the pump beam. This acoustic pulse passes successively through each arm of a grating interferometer, and time-dependent changes in refractive index translate to time-dependent intensity of the interferometrically recombined signal.

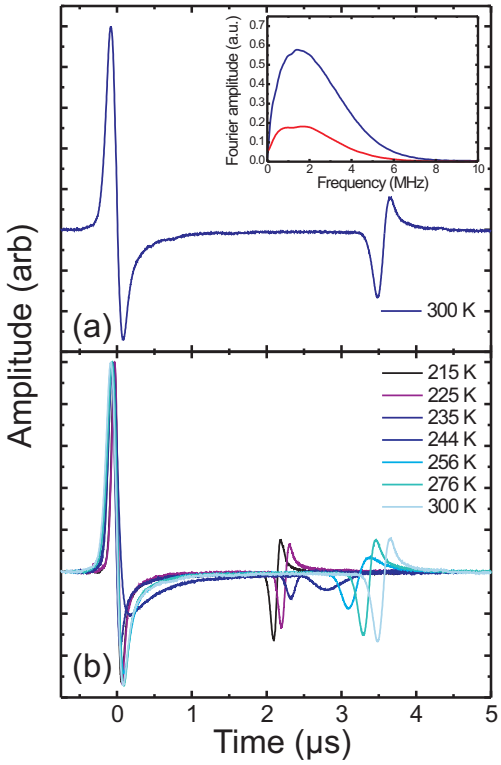


FIG. S10. (a) NAI trace recorded in DC704 at room temperature. A pump pulse is absorbed in the sample, generating a cylindrical wave radiating outwards. We observe the acoustic pulse passing first through one probe point and then through the second, where the amplitude reduction is clearly observed. The inset shows the Fourier amplitude of the pulse at the first (blue curve) and second (red curve) points. (b) Nanosecond acoustic interferometry measurements for different temperatures.

### B. Nanosecond Acoustic Interferometry

In Nanosecond Acoustic Interferometry (NAI) acoustic wavepackets with a distribution of frequency components in the low MHz range are generated by a picosecond duration pump beam loosely focused in the sample. Weak absorption leads to heating and thermal expansion of the excited region, impulsively generating an outward propagating cylindrical wave[S12,S13]. This wave is sequentially detected at the two arms of grating interferometer[S14,S15] due to the phase difference created by density-mediated changes in the refractive index. The interferometer arms are recombined at a diffraction grating, and we measure time-dependent changes in the intensity of the resulting single beam directed to a detector.

The setup is depicted in Fig. S9. To achieve maximum sensitivity, the incoming continuous wave probe beam passes through a polarizing beam splitting cube (PBS) and then a quarter waveplate (QWP) to induce circular polarization. After passing through the diffractive optic (binary phase mask pattern: PM), the $\pm 1$ diffraction orders are brought parallel and focused by a lens through the sample cell to a dichroic mirror at the back of the sample, which reflects the probe beams and transmits the pump. The returning beams recombine at the phase mask, pass again through the QWP, and the resulting single beam is of correct polarization for transmission through the PBS to a fast detector. A glass plate in the path of one interferometer arm was rotated for relative phase control. Signals were recorded at the relative phases $-\pi/2$ and $\pi/2$, midway between maximum constructive and destructive interference, where the induced phase change, and therefore the detected response, was greatest[S15].

Figure S10(a) shows a recorded trace of an acoustic pulse generated in liquid DC704 passing through the first probe arm at $t = 0$ and the second at later times. The inset shows the Fourier amplitude of the pulse at each point, where the attenuation of the wave is apparent through the relative change in spectral amplitude. In Fig. S10(b), we show traces recorded at a number of different sample temperatures for a set of traces normalized to the maximum amplitude.

The effect of the coupling of structural relaxation to the acoustic waves is twofold. First, we observe that as tem-

perature is decreased, the wavepacket arrives at the second probe point more quickly, corresponding to an increasing speed of sound at lower temperatures. Second, we note that the amplitude of the wavepacket has a strong temperature dependence; acoustic damping is relatively low at high temperatures in the liquid state, but as temperature is reduced, strong damping is evident due to the alpha-relaxation. As temperature is decreased further, the alpha-relaxation shifts to lower frequencies and the damping is reduced at the acoustic frequencies of our measurement where we see a solid-like response. We note that even in the absence of acoustic damping, the amplitude of the pulse at the second probe point decreases solely due to the divergent nature of the cylindrical wavepacket, which is accounted for in the analysis below.

The velocity and attenuation of the excited frequency components are determined using the Fourier transform of the acoustic pulse at each detection point according to

$$\tilde{f}(\omega) = \mathcal{F}(f(t)) = \frac{1}{\sqrt{2\pi}} \int_{-\infty}^{\infty} f(t) e^{-i\omega t} dt \,. \tag{S7}$$

Using the shift theorem, i.e., that $\mathcal{F}(f(t-a)) = e^{-i\omega a}\tilde{f}(\omega)$, and the distance $d$ between interferometer probe arms, we can recover the speed of sound for the excited frequency components via the phase. The acquired phase ($\phi$) of the Fourier transform is $\omega a$, and thus by taking the derivative of the phase ($\partial_\omega \phi$) with respect to frequency, we recover the frequency-dependent shift in time $a(\phi)$. Using the Fourier transforms of the wavepacket at the first probe point and second probe point, we can determine the frequency-dependent sound speed via

$$v(\omega) = \frac{d}{\delta t(\omega)} = \frac{d}{\partial_\omega \phi_1(\omega) - \partial_\omega \phi_2(\omega)}. \tag{S8}$$

where the subscripts 1 and 2 refer to the first and second probe point, respectively. In practice, the amplitude of the phase recovered from a numerical Fourier transform may depend on the number of time points in the time-domain trace, and so we needed to multiply Eq. S8 by a constant calibration factor. All recorded traces contained an identical number of time points, and therefore a single calibration factor for all analysis was sufficient. The calibration factor was picked to recover the sound speed of the solid phase determined at low temperatures from the PBG/PSG and ISS data; this calibration factor also recovered the liquid sound speed at high temperatures (in comparison to ISS data), and so we use it with confidence for all temperatures. All points presented here were also collected with the same probe distance $d$, which can be determined using the grating period and the lens focal distance according to

$$d = 2f \tan\left(\sin^{-1}\left(\frac{\lambda_p}{2\Lambda}\right)\right), \tag{S9}$$

where $f$ is the lens focal length, $\lambda_p$ is the probe wavelength, and $\Lambda$ is the grating period. Using our experimental parameters of a 532 nm probe wavelength, 85 mm lens focal length, and 8.5 $\mu$m grating period, this translated to $\sim 5$ mm distance between probe beams which agreed with a physical measurement of the distance.

The frequency-dependent acoustic attenuation $\gamma(\omega)$ can be determined by the amplitude of the Fourier transform of the acoustic pulse at each probe point according to the Beer-Lambert law as

$$\alpha(\omega) = \frac{\ln(|\tilde{f}_2(\omega)|/|\tilde{f}_1(\omega)|)}{d}. \tag{S10}$$

Here $|\tilde{f}_i(\omega)|$ denotes the magnitude and $\phi_i$ denotes the phase of the complex Fourier transform of the acoustic pulse at each point. As we used a round excitation spot to generate cylindrical acoustic waves with a well-defined $r^{-1/2}$ reduction in amplitude, we account for the correction due to the acoustic wave divergence by the constant $A$, which is given in terms of $d$ and the distance between pump spot and probe $d_p$ as

$$A = \sqrt{\frac{d_p + d}{d_p}}. \tag{S11}$$

We note that the attenuation is given here in units of inverse distance, whereas the damping rate is in units of inverse time; conversion between the two can be performed using the speed of sound.

For the broadband spectral analysis we can then construct the complex acoustic modulus by

$$M'(\omega) = \rho v^2(\omega) \frac{1 - \left(\alpha(\omega) v(\omega)/\omega\right)^2}{\left[1 + \left(\alpha(\omega) v(\omega)/\omega\right)^2\right]^2} \tag{S12}$$

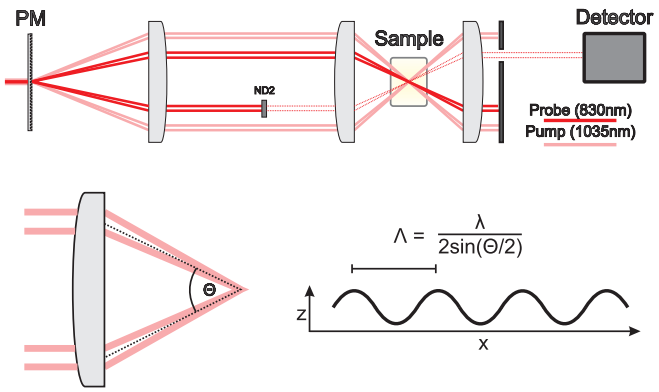


FIG. S11. Schematic illustration of the ISS setup. Both the pump and probe beams are incident on the phase mask (PM) and their ±1 diffraction orders are recombined at the sample at an angle $\theta$.

$$M''(\omega) = 2\rho v^2(\omega) \frac{\alpha(\omega)v(\omega)/\omega}{\left[1 + (\alpha(\omega)v(\omega)/\omega)^2\right]^2}, \tag{S13}$$

which were the quantities used in our analysis below.

Determination of very weak attenuation coefficients becomes unreliable for a particular frequency when the signal-to-noise ratio in the Fourier domain is too low. In practice this was observed when, for a particular frequency in the Fourier domain, the ratio of the magnitude of the difference in acoustic signal amplitudes between the first and second detection points (the amplitude at the second point being corrected by the factor A) and the magnitude of the noise at the second detection point was lower than approximately three to one. For such low attenuation rates, the imaginary part of the modulus could not be determined.

### C. Impulsive stimulated scattering

In an impulsive stimulated scattering (ISS) experiment conducted in a heterodyned four-wave mixing geometry, light from a pulsed laser is incident on a diffractive optical element, typically a binary phase mask (PM) pattern, and split into two parts (±1 diffraction orders; other orders are blocked), which are recombined at an angle $\theta$ as depicted in Fig. S11. The crossed excitation pulses excite an acoustic wave with wavelength $\Lambda$ given by the interference or "transient grating" period

$$\Lambda = \frac{\lambda_e}{2\sin\theta/2} \tag{S14}$$

where $\lambda_e$ is the excitation laser wavelength. Probe light (in the present case from a CW diode laser) is also incident on a phase mask pattern (the same one or another with the same spatial period) and split into two parts, which are recombined at the sample to serve as probe and reference beams. The signal arises from diffraction of probe light off the acoustic wave and any other spatially periodic responses induced by the excitation pulses. The diffracted signal field is superposed with the reference field for heterodyned time-resolved detection of the signal, which typically shows damped acoustic oscillations from which the acoustic frequency $\omega$ and damping rate $\Gamma$ can be determined.

In an experiment where all four beams share common polarization V (denoted VVVV), the action of the excitation pulses is twofold. First, depending upon the absorbance at the pump wavelength, a fraction of the light is absorbed into the sample and this energy is very rapidly converted into heat. Sudden thermal expansion launches counter-propagating acoustic waves with the acoustic period $\Lambda$. In addition to acoustic oscillations, the signal may also show slower, nonoscillatory density responses and thermal diffusion from which complex structural relaxation dynamics and thermal diffusivities may be determined[S16]. This excitation mechanism is labeled Impulsive Stimulated Thermal Scattering (ISTS) and is the dominant mechanism in the VVVV measurements.

The second excitation channel arises from the electrostrictive work done on the liquid by the V-polarized excitations pulses. The electric field of the interference maxima both induces a polarization and does compressive work on the induced dipoles, resulting in impulsive excitation of counterpropagating longitudinal acoustic waves of wavelength $\Lambda$ even in the absence of optical absorption. This excitation mechanism is termed impulsive stimulated Brillouin scattering (ISBS). As the force scales with the gradient of the light intensity, the efficiency of ISBS excitation scales as

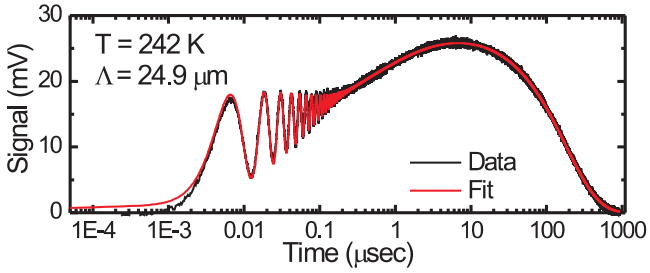


FIG. S12. ISTS signal in DC704 at 242K, 24.9 $\mu$m grating spacing. At short times, there is a damped acoustic oscillation due to counterpropigating acoustic waves. At later times, there is a slow rise due to the alpha-relaxation dynamics revealed though time-dependent thermal expansion. The signal eventually decays due to thermal diffusion of the thermal excitation grating.

the acoustic wavevector $q = 2\pi/\Lambda$. Therefore this mechanism becomes more important as the scattering wavevector is increased.

The excitation pulses may also induce molecular orientational responses that can contribute to signal, analogous to depolarized quasielastic scattering[S7,S17], as well as contributions due to flow. In order to avoid this complication, careful selection of the probe polarization relative to the grating wavevector direction was used to eliminate these contributions to signal.

The signal traces are fit to the model function[S16]

$$A(e^{-t/\tau_{th}} - e^{-\Gamma_A t}\cos(\omega_A t)) + B(e^{-t/\tau_{th}} - e^{-(t/\tau_s)^n}) + Ce^{-\Gamma_A t}\sin(\omega t) \quad \text{(S15)}$$

where $A$ and $B$ are ISTS amplitudes, $C$ is the amplitude for the ISBS signal, $\tau_{th}$ is the thermal decay time, and $\tau_s$ is the characteristic structural relaxation time stretched by the exponent n. Finally, $\omega_A$ is the observed acoustic frequency, and $\Gamma_A$ is the acoustic damping rate. In regimes of extremely low damping, the effect of finite pump and probe spot sizes was explicitly taken into account using the results of Yan and Nelson[S18] via a multiplication of the acoustic damping term by a factor $e^{-\sigma(\omega t/q)^2}$, where $\sigma$ is given terms of the spot sizes of the probe beam $\sigma_p$ and the excitation beam $\sigma_e$ as

$$\sigma = \frac{\sigma_p + 2\sigma_e}{2\sigma_e\,(\sigma_p + \sigma_e)}. \quad \text{(S16)}$$

Figure S12 details a representative trace with $\Lambda = 24.9$ $\mu$m which shows excellent agreement with the model function, Eq. (S15). These data, plotted on a logarithmic time scale to cover signal extending over 6 decades, were taken in the regime where the alpha-relaxation dynamics extend to time scales significantly longer than that of the acoustic response, resulting in insignificant acoustic damping and slow components of thermal expansion that are observed directly in the data. This slow component is represented by the stretched exponential function in the time-domain signal function of Eq. (S15). In principle this slow signal reveals structural relaxation dynamics in the 0.1-100 $\mu$s temporal range and we could equate $\tau_s = \tau_\alpha$. However, in addition to structural relaxation dynamics, this component of the signal includes heat capacity relaxation dynamics that may yield a complicated time-dependent evolution of the sample temperature at the heated interference maxima. We expect that this is a small contribution to the signal, but because we are not able to determine it through independent measurement, we did not use the slow component of our ISS data or the stretched exponential fits to them in construction of our modulus curves.

For this study we focused exclusively on the acoustic contribution. Figure S13 shows three more representative traces of ISTS data recorded with 24.9 $\mu$m grating spacing. In all traces there are oscillations due to counterpropagating acoustic waves. The data in (a) are taken in the high-temperature liquid state, showing weak damping of the acoustic wave. In the regime where the alpha-relaxation is on the time scale of an acoustic period, mechanical energy is quickly dissipated into structural relaxation and the acoustic signal is strongly damped, as shown in (b). Finally, when the liquid is cooled into the very viscous state as in (c), the damping rate is observed to decrease significantly. Here the effects of finite beam spot sizes lead to non-exponential decay, which is modeled by the correction term described above.

The transient grating spacing (*i.e.*, wavevector magnitude $q$) can be varied by changing the phase mask pattern to make the excitation pulses cross at different angles in the sample, and new data can be recorded which will reveal different acoustic frequencies and damping rates as functions of temperature. Using these acoustic parameters determined at many wavevectors at a common temperature, the complex frequency-dependent longitudinal modulus

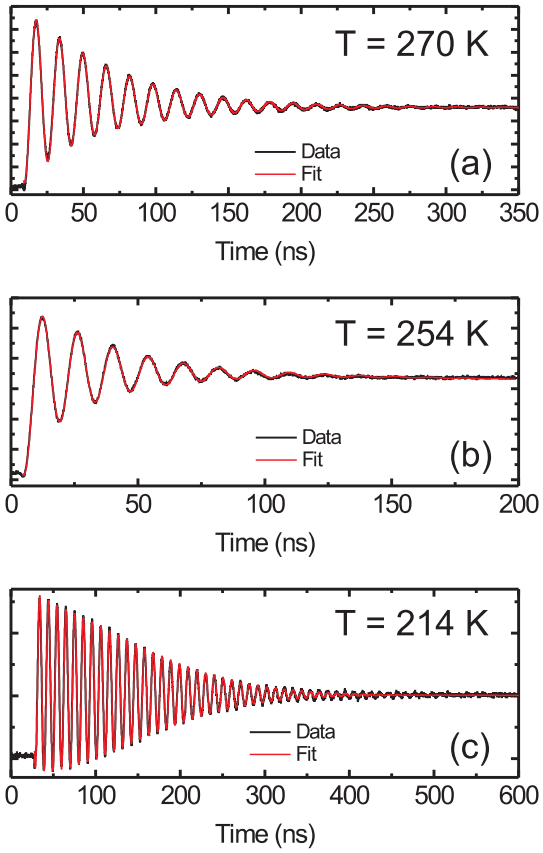


FIG. S13. ISTS signal in different temperature regimes using grating fringe spacing 24.9 $\mu$m. Fits are performed using Eq. S15. In (a), the sample is in the liquid state and damped acoustic oscillations are observed on the sub-$\mu$s timescale. (b) As the sample is cooled, both the frequency and damping rate increase due to the presence of the alpha-relaxation dynamics at the acoustic frequency. (c) Near $T_g$, the acoustic frequency is greatly increased and the damping rate decreased due to the solid characteristic of the material.

$\hat{M}(\omega) = M'(\omega) + iM''(\omega)$ at that temperature can be determined from

$$M'(\omega) = \rho\frac{\omega^2 - \Gamma^2}{q^2} \tag{S17}$$

$$M''(\omega) = \rho\frac{2\omega\Gamma}{q^2}. \tag{S18}$$

The excitation beams were focused to a spot 2.5 mm in the grating dimension and 100 $\mu$m in the perpendicular dimension so that the acoustic waves would have many periods and the decay of signal would be due primarily to acoustic damping rather than propagation away from the excitation and probing region of the sample. In regions of extremely low damping the effects of finite spot size were taken into account, as detailed above. Damping rates as low as 2 $\mu\mathbf{s}^{-1}$ could be measured reliably.

The probe was focused to a spot of 1 mm in the grating dimension by 50 $\mu$m in the perpendicular dimension. We used a common phase mask optimized for diffraction into $\pm 1$ orders at 800 nm for both pump and probe beams. The local oscillator was attenuated by a factor of $10^{-3}$. Approximately 30% of the pump power was lost into zero order with this configuration, but the pump intensity still had to be reduced significantly to avoid unwanted nonlinear effects. The signal was collected with a fast amplified photodiode with 3 GHz bandwidth and processed in a 4 GHz bandwidth digitizing oscilloscope. When slower signals were studied, we used a New Focus Model 1801-FS detector with a bandwidth of DC to 125 MHz. Depending upon signal-to-noise ratios, signals from 2,000 to 4,000 repetitions of the measurement were averaged for each data trace, with total data acquisition times of less than a minute per trace.

The acoustic wavelength was calibrated through ISTS measurements in ethylene glycol, for which the speed of sound is known accurately[S19], and cross-checked with internal measurements of DC704 at high temperature where the speed of sound is constant across the range of measured acoustic wavelengths. This calibration was double-checked after all

of the data collection was finished, and the variation in acoustic wavelength ranged from approximately 0.1% to 1.8%, with an average of 0.7%. This determined our uncertainties in the sound speeds, but did not affect the uncertainties in the damping rate.

To build acoustic spectra, data were taken by fixing the sample temperature and using every available phase mask pattern to provide wavelengths in the range from 1.75 $\mu$m to 101 $\mu$m. These grating spacings were 1.71 $\mu$m, 1.97 $\mu$m, 2.33 $\mu$m, 2.68 $\mu$m, 3.14 $\mu$m, 3.64 $\mu$m, 4.20 $\mu$m, 4.85 $\mu$m, 5.66 $\mu$m, 6.56 $\mu$m, 6.70 $\mu$m, 7.61 $\mu$m, 9.13 $\mu$m, 10.2 $\mu$m, 11.7 $\mu$m, 13.7 $\mu$m, 15.7 $\mu$m, 18.3 $\mu$m, 21.3 $\mu$m, 24.9 $\mu$m, 28.5 $\mu$m, 33.0 $\mu$m, 38.1 $\mu$m, 44.2 $\mu$m, 49.8 $\mu$m, 50.7 $\mu$m, 56.9 $\mu$m, 65.9 $\mu$m, 76.0 $\mu$m, 88.0 $\mu$m, and 101 $\mu$m. The procedure was repeated for different temperatures until the desired range was covered.

### D. Time-Domain Brillouin Scattering (∼3–23 GHz)

In time-domain Brillouin scattering (TDBS), acoustic wave propagation at low GHz frequencies is monitored by an optical, time delayed probe at a fixed wave vector and a complex frequency is measured. The detection scheme is based on the coupling of mechanical strain with laser light through the so-called photoelastic or Brillouin effect.

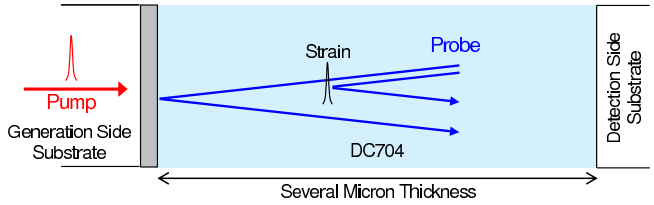


FIG. S14. Schematic diagram of time domain Brillouin scattering detection. An acoustic strain pulse is generated in a transducer film and propagates into an adjacent liquid layer. Incident probe light reflects off of the transducer film, but also off the propagating strain pulse due to acoustically induced local changes in the refractive index, and interference gives rise to an oscillatory modulation of the overall reflected probe intensity.

A schematic illustration of this technique is shown in Figure S14. Acoustic waves are excited by a sub-picosecond optical pump pulse which deposits energy in a photo-acoustic aluminum transducer thin film. The subsequent sudden thermal expansion launches an acoustic strain pulse $\eta(z,t)$ into the adjacent liquid film. Probing of the propagation and attenuation of the strain pulse away from the transducer is accomplished by a second optical pulse mechanically delayed by a variable time $\Delta t$ relative to the pump. The reflected probe light consists of a number of superposing beams with a principal reflection from the transducer and minor reflections from the strain pulse[S9,S20]. These reflections arise from the local change in refractive index produced by the presence of the strain pulse via the photoelastic or Brillouin effect. Depending on the distance $d = c\Delta t$ of the strain pulse from the transducer film, the reflected beams interfere either constructively or destructively. This results in an oscillatory modulation of the total reflected intensity as a function of time, which can be used to determine the acoustic speed $c$ of the strain pulse in the sample while the amplitude of the modulation can be related to the amplitude of the strain.

At normal incidence of the probe beam with respect to the transducer, the measured Brillouin scattering frequency is

$$f_{BS} = \frac{2nc}{\lambda}\,, \tag{S19}$$

where $n$ is the index of refraction and $\lambda$ is the optical wavelength. A measurement of this frequency can thus give the sound velocity when the refractive index of the sample is known. To determine the acoustic attenuation rate at this frequency, the raw data were fit to the time-domain form of a damped oscillator, i.e., $e^{-\Gamma t}\sin(\omega t)$.

For the purpose of compiling broad relaxation spectra, we recorded time-domain Brillouin scattering data at many different temperatures with probe light at the laser fundamental wavelength, centered at 790 nm, and frequency doubled light, centered at 395 nm. The sample was constructed from a 20 nm aluminum transducer film on a sapphire generation-side substrate and a many-micron thick liquid layer held by another sapphire substrate. This construction allowed us to monitor the propagation of the acoustic strain pulse until it was attenuated to below our detection limit.

Selected raw data at several different temperatures are shown in Figure S15 and clearly illustrate the strong acoustic attenuation at temperatures above the glass transition temperature, $T_g = 210$ K. The attenuation rate is observed to decrease as the liquid is cooled into the glassy state. Results for the extracted Brillouin scattering frequency and attenuation rate were obtained by fitting a Lorentzian oscillator as described above.

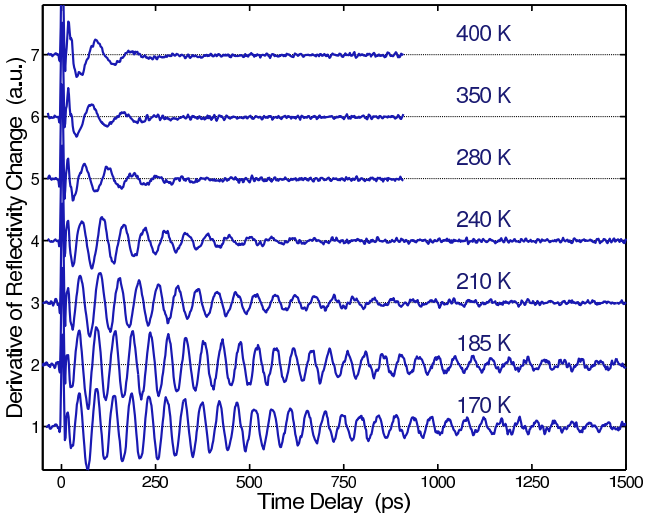


FIG. S15. Selection of Brillouin scattering data in DC704 recorded at various temperatures. At the highest temperatures, the frequency is lower and the damping rate higher due to the presence of complex relaxation dynamics at the probed frequency. As the temperature is reduced, the frequency is observed to increase and the damping rate is observed to decrease significantly.

### E. Picosecond Ultrasonic Interferometry (~25-120 GHz)

Here we describe the manner in which a specialized picosecond laser ultrasonic technique may be combined with interferometric detection for probing longitudinal acoustic waves in the tens to hundreds of gigahertz frequency range. This method, depicted in Fig. S16, is performed in a similar sample geometry as in time-domain Brillouin scattering. Single-cycle acoustic waves are generated in a thin metal transducer film on one side of a liquid film and their arrival and shape is measured by a Sagnac interferometer[S21,S22] at the receiver metal film. In our analysis we compared transmitted strain pulses through different liquid thicknesses with each other in order to extract the liquid response at a fixed frequency.

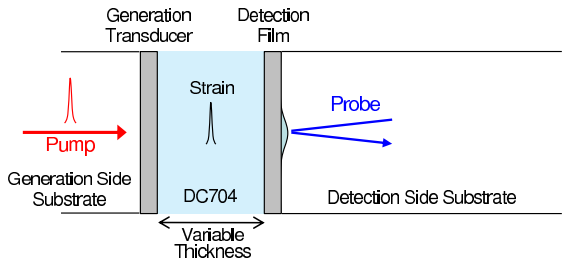


FIG. S16. Sketch of picosecond ultrasonic interferometric experimental approach. Energy deposition by an ultra-short laser pulse in a transducer film resulted in sudden thermal expansion and launched a compressional strain pulse into and through the DC704 liquid sample. Its arrival in a detection film caused a small displacement of that film which was detected interferometrically.

Our approach is to compare signals transmitted through different thicknesses of sample material. In a manner similar to the NAI experiment detailed in Sec. I B, we compare the amplitudes and phases at a given frequency by Fourier transformation of the two time-domain signals $h_1(t)$ and $h_2(t)$, which constitute two signals transmitted through different sample thicknesses $d_1$ and $d_2 > d_1$ (e.g., $\eta_4$ and $\eta_{10}$ in Fig. S17).

Figure S17(a) shows a selection of the measured displacements for several different thicknesses of DC704. Typically, we measured the strain transmitted through about 50 different liquid thicknesses. A signal ($\eta_0$) from the part of the sample assembly where the transducer films were in contact is added to the plot. We did not use such signal amplitudes for our analysis since the acoustic strain in this case did not experience exactly the same conditions (due to the contact between the metal thin films) as in the other cases, but the signal provided calibration for essentially zero liquid thickness.

We assume that the displacement can be described by a plane wave equation. The time-derivative of the displace-

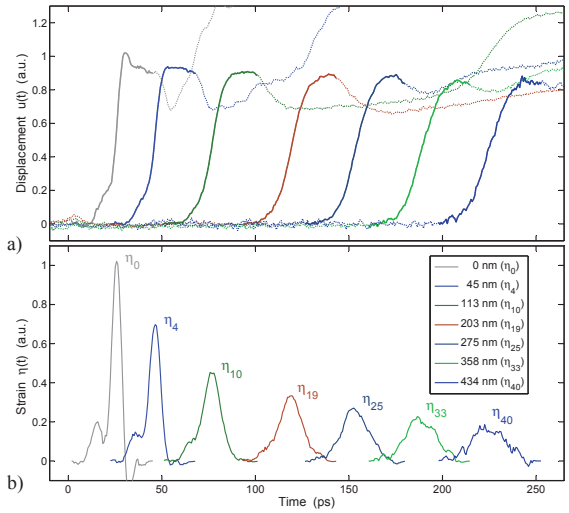


FIG. S17. Measured and normalized displacement data (a) and the derived strain (b) after transmission through different layer thicknesses of DC704 at 200 K. The acoustic strain was produced by a 30 nm aluminum transducer film on a sapphire generation side substrate and detected interferometrically at the back side of a 100 nm aluminum film on a sapphire detection side substrate. Signals labeled $\eta_4$, $\eta_{10}$, $\eta_{19}$, $\eta_{25}$, $\eta_{33}$, and $\eta_{40}$ are from acoustic waves transmitted through progressively greater liquid thicknesses as indicated.

ment $u(t,x)$ is then proportional to the strain $\eta(t,x)$,

$$\eta(t,x) = \frac{d}{dx}u(t,x) \;=\; \frac{1}{c}\frac{d}{dt}u(t,x)\;. \tag{S20}$$

where $c$ is the acoustic phase velocity (assuming $c$ is non-dispersive).

Figure S17(b) shows the transmitted strain through a selection of different liquid thicknesses, labeled $\eta_4$, $\eta_{10}$, $\eta_{19}$, $\eta_{25}$, $\eta_{33}$, and $\eta_{40}$. The shape of the strain after transmission through different liquid thicknesses is simply related to a set of acoustic parameters which includes the complex speed of sound or equivalently the complex longitudinal modulus. After traveling through an additional distance $\Delta d$ in the liquid, the Fourier domain 'output' strain $\tilde{\eta}_{out}(\omega)$ is related to the 'input' strain $\tilde{\eta}_{in}(\omega)$ by the complex wavevector, $k(\omega) = \omega/c(\omega)$,

$$\tilde{\eta}_{out}(\omega) = e^{i\hat{k}(\omega)\Delta d}\;\tilde{\eta}_{in}(\omega)\;. \tag{S21}$$

While the real portion of the wavevector shifts the phase of the input strain, the imaginary component of the wavevector dampens the amplitude. If we denote the transmitted strain as

$$\tilde{\eta}_{trans}(\omega) = \frac{\tilde{\eta}_{out}(\omega)}{\tilde{\eta}_{in}(\omega)}\;, \tag{S22}$$

we can write the complex acoustic velocity as

$$c(\omega) = \frac{\omega}{k} \;=\; \frac{i\,\omega\,\Delta d}{\ln(\tilde{\eta}_{trans}(\omega))}\;. \tag{S23}$$

From this, the complex acoustic modulus $M(\omega)$ and the acoustic compliance spectrum $J(\omega)$ can be determined directly from a broadband measurement of the transmitted strain:

$$M(\omega) = -\rho\left[\frac{\omega\,\Delta d}{\ln(\tilde{\eta}_{trans}(\omega))}\right]^2\;. \tag{S24}$$

In order to account for different attenuation strengths at different frequencies in the most reliable manner, we conducted our analysis on data sets having about 50 strain profiles, each recorded at a different liquid thickness using a fixed excitation pulse shape and at a constant sample temperature.

## II. ANALYSIS OF MECHANICAL SPECTRA

Below we provide a more in-depth discussion of some of the fitting results presented in the main manuscript in the context of the mode coupling theory.

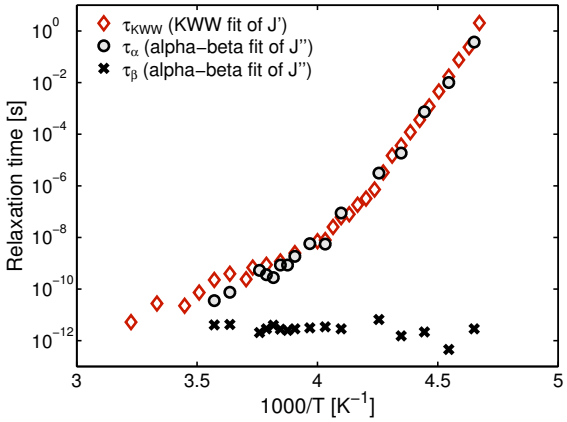


FIG. S18. Relaxation times of the alpha and beta processes from fits of data to a phenomenological alpha-beta merging model expressed as a network diagram[S25,S27]. The alpha relaxation times of the alpha-beta model are markedly non-Arrhenius and agree well with the $\tau_\alpha(t)$ values of the stretched exponential fit. The beta relaxation time is roughly temperature-independent.

### A. Time-temperature superposition

The relaxation behavior at frequencies around the alpha-peak was fitted by a stretched exponential equation

$$\chi(t) = \chi_0 + \Delta\chi \exp\left(-(t/\tau_\alpha)^n\right) , \tag{S25}$$

where $\chi_0$ denotes the long-time limit of $\chi(t)$ and $\Delta J\chi = \chi_0 - \chi_\infty$ the relaxation strength.

The $M''(\omega)$ data were fitted to a numerical Fourier transform of Eq. (S25) using a routine developed by Wuttke[S23], yielding the fits to the data in Fig. 2(a) of the main text. The compliance data $J'(\omega)$ and $J''(\omega)$ were also fit to the KWW Fourier transform using the same routine. In order to demonstrate TTS, rescaling of the compliance data was accomplished using our measured values for the limiting instantaneous speed of sound ($c_\infty$)[S24] whose temperature dependence was found to be fit well by the form

$$c_\infty(T) = 3840[\mathrm{m/s}] - 6.9[\mathrm{m/sK}] \times T \tag{S26}$$

to calculate $J_\infty = \sqrt{\rho/c_\infty}$ and the normalized quantities in Fig. 3(a).

The low-temperature compliance data cover the alpha relaxation spectrum quite thoroughly, and the alpha spectra were found to be fit well by the KWW form with the stretching exponent $n = 0.5$. This value was fixed for the fits at higher temperatures, leaving only the three remaining fitting parameters $J_0$, $\Delta J$, and $\tau_\alpha$. Restricting the number of fitting parameters made possible fitting of spectra across the modest frequency gaps in our spectra. We note that the measurements were typically conducted with small temperature steps (usually $\sim 2$ K) but the measurements conducted with different methods were not all made at exactly the same temperatures. In order to show results spanning the entire frequency range at selected temperatures (e.g., 215 K, 225 K, and 235 K in Fig. 3a), we interpolated at the lower frequencies between data measured at very nearby temperatures, e.g., 214 K and 216 K for the results shown at 215 K. This procedure allowed us to reliably connect results from our highest to lowest frequency ranges despite the number of measurement methods involved.

The KWW form describes only alpha relaxation, not the faster beta relaxation dynamics which clearly appear in the imaginary compliance spectra $J''(\omega)$ at high frequencies. In order to extend our fits to this part of the spectra, we used an alpha-beta merging model that has been described elsewhere[S25,S26]. The fitted alpha and beta relaxation times from this model are shown in in Fig. S18. The alpha relaxation times show excellent agreement with the $\tau_\alpha$ values obtained from the stretched exponential fits. The beta relaxation time is nearly constant over the range of temperatures explored here, i.e., $\tau_\beta \sim 1$ ps, as expected. Although the alpha-beta model fits were not used to test MCT, they can provide insights based on their parameter values and on their implications for the connections between the real and imaginary parts of the compliance. Both the KWW and the alpha-beta fits are illustrated in Fig. S19 for a single temperature, 275 K. The alpha-beta model fit overshoots the real part dramatically at the highest frequencies. However, the resonance region is approached here, and we can add this to our alpha-beta model and obtain a curve that matches the rise in the imaginary part while the real part remains flat. This is shown in Fig. S19 in red. The fit is not perfect; the purpose here is merely to show that although beta relaxation is apparent in the imaginary spectrum only, the data do not violate the Kramers-Kronig relations. Owing to the consistency of the KWW fitting scheme

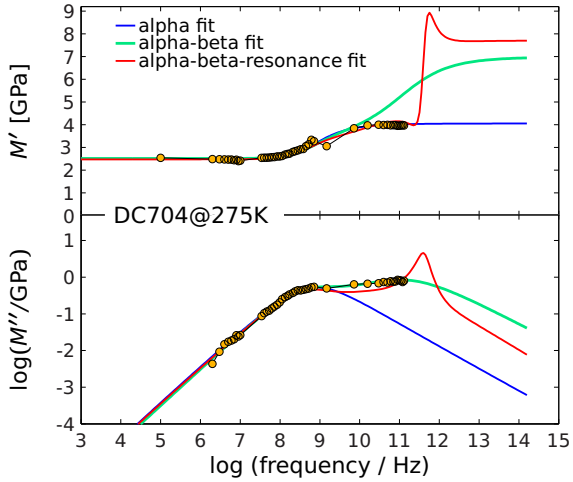


FIG. S19. The complex longitudinal modulus of DC704 at 275 K including several fitting schemes: the blue curve is a stretched exponential (Eq. (S25)) fit of the real part, the green curve is an alpha-beta model fit[S25,S26] to the imaginary part, and the red curve is a an alpha-beta model fit with an added resonance.

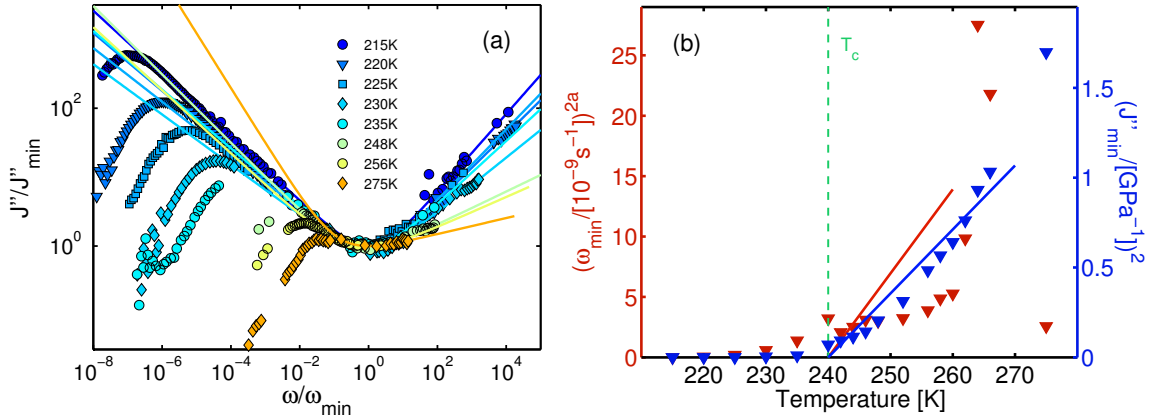


FIG. S20. Test of mode-coupling theory predictions for the evolution of the susceptibility minimum $J''_{\rm min}(\omega_{\rm min})$. (a) $J''(\omega)$ rescaled at the susceptibility minimum. The fits are given to the asymptotic form given by Eq. (3) of the main text. (b) $(\omega_{\rm min})^{2a}$ and $(J''_{\rm min})^2$ vs $T$. $T_c = 240$ K is marked by the vertical dashed line, and linear fits (keeping $T_c$ fixed) to temperatures in the range from 240 K to 248 K are shown as solid lines.

with the alpha-beta analysis, as shown in Fig. S18, the KWW fits were used in Fig. 3(b) of the main text and the subsequent analysis.

### B. Temperature dependent compliance minimum values

Using the fits described in the previous section, the imaginary compliance $J''(\omega)$ plots may be superposed upon each other by scaling the axes by the frequency minimum $\omega_{\rm min}$ and the imaginary compliance value $J''_{\rm min}$, shown in Fig. S20(a). The determined frequencies $\omega_{\rm min}(T)$ and compliance values $J''_{\rm min}(T)$ at the minima between the alpha and beta relaxation features may be used in conjunction with the dynamic exponent $a$ to test additional MCT predictions. These predictions indicate the scaling of the imaginary susceptibility minimum as $\chi''(\omega_{\rm min}) \propto |T - T_c|^{1/2}$ and of the minimum frequency as $\omega_{\rm min} \propto |T - T_c|^{1/2a}$. In Fig. S20(b) we plot both $(J''_{\rm min})^2$ and $(\omega_{\rm min}(T))^{2a}$ versus temperature. The lines shown are the predictions of MCT based on the value $T_c = 240$ K. As in Figs. 5(b)–5(d) of the main paper, the parameters can be determined over a wide temperature range, but only the 240–248 K range is useful for comparison to MCT predictions. However, the uncertainties in $\omega_{\rm min}$ and $J''_{\rm min}$ make this assessment difficult.

[S1]T. Hecksher, N. B. Olsen, K. A. Nelson, J. C. Dyre, and T. Christensen, J. Chem. Phys. **138**, 12A543 (2013)
.

[S2]T. Christensen and N. B. Olsen, Phys. Rev. B **49**, 15396 (1994)
.

[S3]T. Christensen and N. B. Olsen, Rev. Sci. Instrum. **66**, 5019 (1995)
.

[S4]T. Hecksher, *Relaxation in supercooled liquids.*, Ph.D. thesis, Roskilde University (2010)
.

[S5]J. A. Johnson, *Optical Characterization of Complex Mechanical and Thermal Transport Properties*, Ph.D. thesis, Massachusetts Institute of Technology (2011)
.

[S6]Y.-X. Yan and K. A. Nelson, J. Chem. Phys. **87**, 6257 (1987)
.

[S7]S. M. Silence, A. R. Duggal, L. Dhar, and K. A. Nelson, J. Chem. Phys. **96**, 5448 (1992)
.

[S8]D. H. Torchinsky, *Optical Study of Shear and Longitudinal Acoustic Waves and Complex Relaxation Dynamics of Glass Forming Liquids*, PhD thesis, Massachusetts Institute of Technology, Cambridge, MA (2008)
.

[S9]C. Thomsen, H. Grahn, H. Maris, and J. Tauc, Phys. Rev. B **34**, 4129 (1986)
.

[S10]C. Klieber, *Ultrafast photo-acoustic spectroscopy of supercooled liquids*, Ph.D. thesis, Massachusetts Institute of Technology (2010)
.

[S11]J. D. Choi, T. Feurer, M. Yamaguchi, B. Paxton, and K. A. Nelson, Appl. Phys. Lett. **87**, 081907 (2005)
.

[S12]C. K. N. Patel and A. C. Tam, Rev. Mod. Phys **53**, 517 (1981)
.

[S13]A. Neubrand and P. Hess, J. Appl. Phys. **71**, 227 (1992)
.

[S14]P. Hess, App. Surf. Sci. **106**, 429 (1996)
.

[S15]C. Glorieux, J. D. Beers, E. H. Bentefour, K. V. de Rostyne, and K. A. Nelson, Rev. Sci. Instr. , 2906 (2004)
.

[S16]Y. Yang and K. A. Nelson, J. Chem. Phys. **103**, 7722 (1995)
.

[S17]G. Hinze, D. D. Brace, S. D. Gottke, and M. D. Fayer, J. Chem. Phys. **113**, 3723 (2000)
.

[S18]Y.-X. Yan and K. A. Nelson, J. Chem. Phys. **87**, 6240 (1987)
.

[S19]S. Silence, Ph.D. thesis, Massachusetts Institute of Technology (1991)
.

[S20]H. N. Lin, R. J. Stoner, H. J. Maris, and J. Tauc, J. Appl. Phys. **69**, 3816 (1991)
.

[S21]D. H. Hurley and O. B. Wright, Opt. Lett. **24**, 1305(3) (1999)
.

[S22]B. Perrin, C. Rossignol, B. Bonello, and J. Jeannet, Physica B: Cond. Matter **263-264**, 571 (1999)
.

[S23]J. Wuttke, Algorithms **5**, 604 (2012)
.

[S24]C. Klieber, T. Hecksher, T. Pezeril, D. H. Torchinsky, J. C. Dyre, and K. A. Nelson, J. Chem. Phys. **138**, 12A544 (2013)
.

[S25]N. Saglanmak, A. I. Nielsen, N. B. Olsen, J. C. Dyre, and K. Niss, J. Chem. Phys. **132**, 024503 (2010)
.

[S26]B. Jakobsen, K. Niss, C. Maggi, N. B. Olsen, T. Christensen, and J. C. Dyre, J. Non-Cryst. Solids **357**, 267 (2011)
.

[S27]B. Jakobsen, T. Hecksher, T. Christensen, N. B. Olsen, J. C. Dyre, and K. Niss, J. Chem. Phys. **136**, 081102 (2012).